A study and development of real-time strontium-90 counters based on Cherenkov radiation detection

July 2017

Hiroshi Ito

Graduate School of Science

CHIBA UNIVERSITY

（千葉大学学位申請論文）

A study and development of real-time strontium-90 counters based on Cherenkov radiation detection

2017 年 7 月

千葉大学大学院 理学研究科

基盤理学専攻 物理学コース

伊藤 博士

Abstract

In this thesis work, a new type of detector was developed in order to measure strontium-90 (^{90}Sr) in real time. This detector based on Cherenkov radiation detection can measure a radioactivity concentration of ^{90}Sr in a test sample, e.g., food or water, within measuring time of one hour. A novel method to read Cherenkov light from an aerogel radiator via wavelength-shifting fibers was adopted. I studied the basic mechanism of the detection of Cherenkov photons from silica aerogel via wavelength-shifting fibers. The light collection efficiency for the fibers to absorb Cherenkov photons was estimated by several test experiments and simulation calculations. By using this technology, the effective area of inspection could be extracted while suppressing accidental noise due to radiation such as γ rays from radioactive isotopes in the sample. I studied the background from environmental radiation and its influence on the detector performance. Although the result suggested the existence of bismuth-214 (^{214}Bi) (a radon progeny) in the air, it was found that the impact can be negligible. I produced a prototype detector. It consists of a threshold-type Cherenkov detector using silica aerogel with refractive index of 1.0411 and light guides by means of wavelength-shifting fibers, a trigger counter using scintillating fibers, cosmic-ray veto counters using plastic scintillators, and external lead and brass shielding blocks. The effective area was 300×100 mm^2. The detector performance was estimated using radioactive sources, ^{90}Sr, caesium-137 (^{137}Cs), and potassium-40 (^{40}K). The "signal model" was developed to reproduce detector performance and detection efficiency was estimated with the simulated ^{90}Sr signal of a few Bq. The detection limit achieved 46 kg/Bq for a dried seafood sample at one-hour measurement in the detector. This value is lower than the contamination allowance of 100 Bq/kg in food specified by the Ministry of Health, Labour and Welfare, Japan, in 2012. The developed detector can be applied to the official real time inspection of ^{90}Sr contamination.

Acknowledgements

I thank to Prof. Hideyuki Kawai of Chiba University for providing not only this study but also various precious experiences for a long term of 5 years.

I thank to Prof. Sigeru Yoshida, and Asst. Prof. Keiichi Mase of Chiba University for providing a chance of this study.

I thank to Dr. Makoto Tabata of Chiba University for providing silica aerogel tiles, teaching how to research, and suggesting in this study.

I thank to Prof. Jun Imazato and Dr. Yoichi Igarashi of High Energy Accelerator Organization, Japan, Prof. M. D. Hasinoff of University of British Columbia, Canada, Asst. Prof. Suguru Shimizu and Dr. Keito Horie of Osaka University, Asst. Prof. Takatugu Ishikawa of Tohoku University for grate advices and suggestions.

I thank to Mr. Satoshi Kodama, Mr. Munetaka Nitta, Mr. Atsushi Kobayashi, Mr. Takahiro Mizuno, Mr. Hiroyuki Kobayashi, Mr. Taichi Nakamura, Mr. Yusaku Emoto, Mr. Shota Kimura, Mr. Kenta Fujihara, and Mr. Kentaro Kurusu of our good laboratory members in Chiba University, for their cooperation.

Finally, I thank to my friends and my family for their special supports.

Contents

List of Figures

List of Tables

Chapter 1

Introduction

A severe nuclear accident occurred at the Fukushima Daiichi Nuclear Plant in March, 2011, and radioisotopes spread around Japan and over the Pacific Ocean [1]. There is still a problem of radioactivity contamination of seafood by long-lives isotopes such as ^{137}Cs and ^{90}Sr even 6 years after the accident. [2, 3].

In the decay chain of ^{90}Sr$\rightarrow^{90}$Y$\rightarrow^{90}$Zr, ^{90}Sr decays to ^{90}Y by emitting a β ray (maximum energy of $K_{\max} = 0.54$ MeV) with a half life of 28.8 yr and the daughter (^{90}Y) decays further to ^{90}Zr by emitting a β ray ($K_{\max} = 2.28$ MeV) with a half life of 64 h [4]. The β-ray energy spectrum from this decay chain is shown in Fig. 1.1. There is a radioactive equilibrium already to decay due to shorter life time of ^{90}Y, and the radioactivity of ^{90}Y is close to that of ^{90}Sr. The International Commission on Radiological Protection (ICRP) estimated the effective dose coefficient of ^{90}Sr (^{90}Y) and ^{137}Cs for adults to be 2.4×10^{-8} Sv/Bq and 4.6×10^{-9} Sv/Bq, respectively [5]. Strontium is an alkali earth metal (same as calcium) and tends to accumulate in the bone and remain there for long time. In the red marrow, the dose coefficients of ^{90}Sr and ^{137}Cs were estimated as 1.6×10^{-7} Sv/Bq and 4.4×10^{-9} Sv/Bq, respectively, namely the coefficient of ^{90}Sr is 36 times higher than ^{137}Cs. This ratio increases with decreasing age, reaching an estimated maximum value of 126 in infants [5].

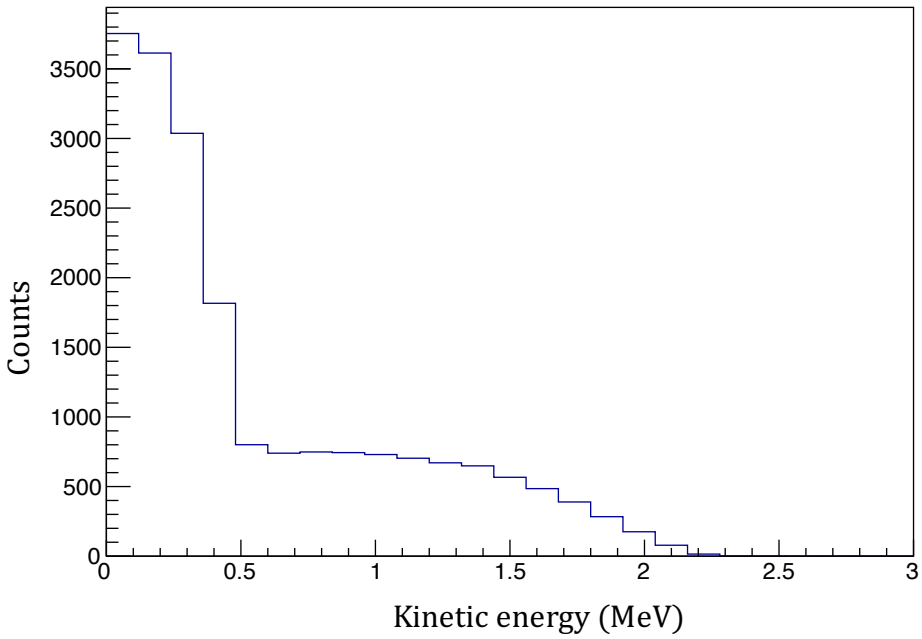

Fig. 1.1: Energy spectrum of β ray from ^{90}Sr and ^{90}Y.

1.1 Conventional method of ^{90}Sr radioactivity measurement

The conventional method of measurement of ^{90}Sr concentration is based on chemical extraction after a sample is burned and becomes ash, and it usually takes a few weeks or one month [6]. Therefore, it is required to improve the contamination inspection in the case of raw-fresh foods. Recent studies have been focusing on the method to measure the radioactivity concentration of ^{90}Sr rapidly in real time [7].

In the methods to measure the end-point of the ^{90}Y β-rays energy spectrum using a calorimeter or a magnetic spectrometer, it is very difficult to identify the end point in the presence of cosmic rays and environmental radiations [8]. In the range measurement method, the detection is limited by accidental backgrounds. It was reported that the detection limit for ^{90}Sr concentration is a few Bq/g in a 10-min measurement in water, which corresponds to 500-1,000 Bq/kg for a one-hour measurement [7, 9].

A method of ^{90}Sr radioactivity measurement based on Cherenkov radi-

ation was reported [10], in which the detection efficiency of ^{137}Cs was suppressed to (2–4)$\times 10^{-2}$ in comparison with that of ^{90}Sr by using a silica aerogel radiator with a refractive index of $n = 1.047$ and a cosmic-ray veto counter [11–14]. The detection efficiency was 0.024 in a 3-hour measurement and the detection limit of 0.3 Bq was determined for an effective area of 5×5 cm^2 [14].

1.2 This study and motivations

In the present work, I developed a threshold-type Cherenkov detector to measure ^{90}Sr concentration based on using a silica aerogel but with wavelength-shifting fiber light readout in order to achieve higher sensitivity to ^{90}Y β rays than to other β and γ rays in a shorter measurement time of one hour, practically in real time.

In the conventional detector, a photomultiplier tube (PMT) was set on one end of the aerogel radiator. The PMT is exposed to β or γ rays from other radionuclides in the sample or in the environment giving rise to accidental backgrounds. In the present study, a challenging scheme to install a Cherenkov detector system using wavelength-shifting fiber light readout was proposed in order to suppress such noises. Although the detection efficiency of ^{90}Sr is reduced by using the fibers, this study aims to detect only β rays from ^{90}Y by the suppressing other accidental background substantially.

The β rays from ^{90}Y emit Cherenkov photons in the aerogel with energy loss. The number of emitted photons was made clear, the light collection efficiency in the wavelength-shifting fibers light guide was determined, and the final number of photoelectrons observed in the PMT was measured in this study.

As an environmental natural radioactivity, ^{214}Bi which is one of the radon progenies emits β rays with $K_{\max} = 3.27$ MeV. Its influence the detector on was investigated by measuring the ^{214}Bi concentration on the sample surface and in the air.

The prototype detector was produced together with cosmic-ray veto counters on the top and four sides. The detector performance was estimated using radioactive sources. The ^{90}Sr source had a radioactivity of 23–24 kBq. The behaviour of the output signal from the detector for the source was investigated and a "signal model " was developed to reproduce the performance. The detection efficiency corresponding to a few Bq ^{90}Sr source and a lower

limit of radioactivity were estimated by using this model.

This thesis presents (1) a basic concept of the aerogel Cherenkov detector using wavelength-shifting fibers, (2) the investigation of the effect of background from the environment, (3) the prototype detector structure and specifications, and (4) the performance of prototype detector.

Chapter 2

Basic concept of an aerogel Cherenkov detector using wavelength-shifting fibers

In this Chapter, the basic principle of the threshold-type aerogel Cherenkov detector is presented and the functions of the components are described. The light collection efficiency of the wavelength-shifting fibers for Cherenkov photons was estimated in a cosmic-ray test and simulation calculation. The suppression of accidental noise using the fibers was studied with radioactive sources.

2.1 Cherenkov radiation

When a charged particle passes through matter of refractive index n with a velocity v faster than the light velocity c/n, photons are emitted in the direction with an opening angle $\theta_{\rm C}$ from the particle path. The Cherenkov angle $\theta_{\rm C}$ is given as $\cos\theta_{\rm C} = c/vn$. Thus, there is a threshold for velocity v or index n for the Cherenkov radiation.

The relation between the kinetic energy K of a β ray and the threshold of refractive index $n_{\rm th}$ is given as

$$\begin{aligned} n_{\rm th} = \frac{c}{v} &= \frac{E}{pc} \\ &= \frac{m_{\rm e}c^2 + K}{\sqrt{(m_{\rm e}c^2+K)^2 - m_{\rm e}^2c^4}}, \end{aligned} \tag{2.1}$$

where m_e is the electron mass. This threshold condition for β rays from ^{40}K with $K_{\max} = 1.31$ MeV is $n_{\rm th} = 1.041$. If $n > n_{\rm th}$, the most serious source of background may be ^{40}K because potassium is commonly contained in most samples in nature.

The number of Cherenkov photons is given as

$$N = 2\pi\alpha L \left(1 - \frac{1}{n^2\beta^2}\right) \int_{200\ \rm nm}^{800\ \rm nm} \frac{d\lambda}{\lambda^2}, \tag{2.2}$$

where α is the fine-structure constant, L is the radiator matter thickness that the electron passes through, $\beta = v/c$, λ is the wavelength of emitted photons, and the integrated region is the range from the near ultra-violet (UV) to visible-light (200–800 nm).

2.2 Silica aerogel

To satisfy this requirement for the Cherenkov condition, silica aerogel was adopted as the radiator, which is SiO_2 and has a low density, a low refractive index, and high transparency for visible light. The aerogel with a refractive index of 1.003–1.25 can be produced by controlling the volume ratio of SiO_2 and air [15–18]. Further, aerogel without a hydrophilic property was developed by a hydrophobic treatment [19], thus constant density and refractive index for a long term of dozen years were obtained.

Cherenkov photons have a spectrum inversely proportional to the square of wavelength (Eq. 2.2). However, aerogel has a lower transmittance in the near UV range (200–380 nm). These spectra are shown in Fig. 2.1. The green line is the original Cherenkov spectrum normalized to 1 at 200 nm. The black lines are the transmittance $T(\lambda)$ depending on the wavelength for the aerogel thickness of 1–6 cm. It is given as

$$T(\lambda) = A \exp\left(\frac{-Ct}{\lambda^4}\right), \tag{2.3}$$

where A is the amplitude ($A = 1$), $C = 5.33 \pm 0.03\ \mu{\rm m}^4/{\rm cm}$ [19], t = 1–6 cm is the thickness of the aerogel. It is mentioned that this transmittance indicates the percentage of photons going straight ahead, in which optical absorption and scattering in the aerogel is not considered individually. The red lines are the spectra of Cherenkov photons passing through the depth of 1–6

cm in the aerogel. This is calculated as the product of the original Cherenkov spectrum and the transmittance. Therefore, the effective Cherenkov photons spectrum has a peak at 300–500 nm. This spectrum curve is used in a simulation to understand the optical collection efficiency of the wavelength-shifting fibers.

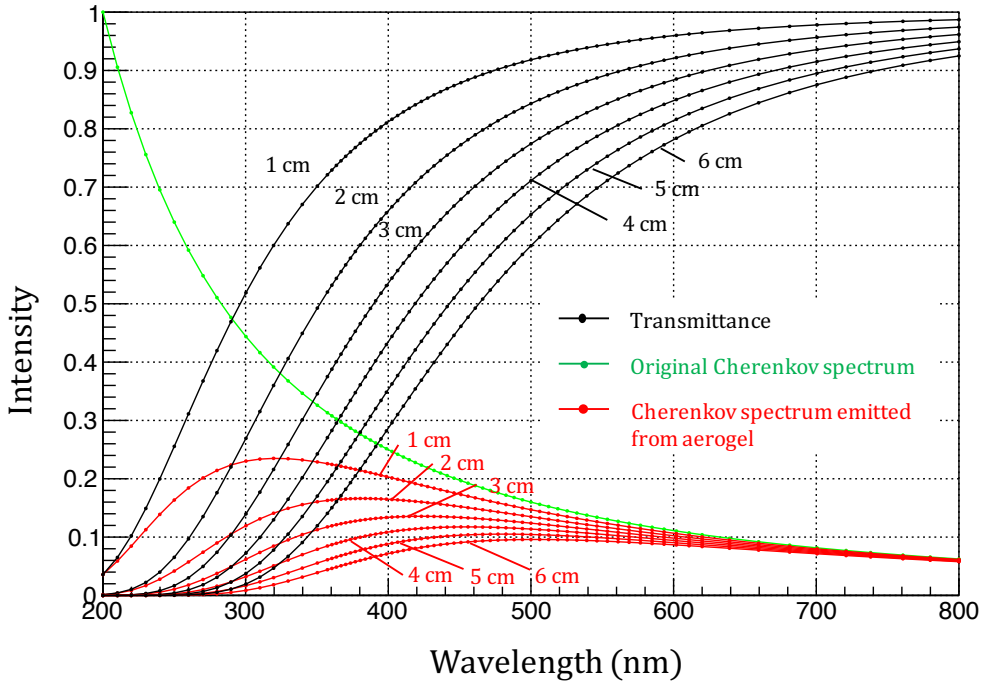

Fig. 2.1: The original Cherenkov spectrum (green), transmittances for aerogel thickness t = 1–6 cm (black), and spectra of effective Cherenkov photons emerging from the aerogel of 1–6 cm (red).

2.3 Wavelength-shifting fibers

A wavelength-shifting fiber is an optical plastic fiber including wavelength-shifter in the core. The wavelength of the Cherenkov photon entering the fiber is red-shifted and the photon is re-emitted isotopically. The photons satisfying the total reflection condition at the boundary between the core and the cladding are propagated to the ends of fibers and observed by PMTs.

A typical fiber has a single cladding structure. Because the refractive indices of the core (with polystyrene) and the cladding (with polymethylmethacrylate) are 1.59 and 1.49, respectively, the critical angle is 69.6° according to the Snell-Descartes law (the law of refraction). As a consequence, the percentage satisfying the total reflection condition in re-emitted photons is 6.2%, which is defined as the trapping efficiency. A double cladding fiber has an outer cladding structure (fluorinated polymer with a refractive index of 1.42) in addition to the single cladding structure, with a result of higher trapping efficiency of 10.8% (with a critical angle of 72.4°). Thus, the double cladding fibers were used, for which the trapping efficiency is approximately 1.74 times higher than in the single cladding fibers.

In this study, two-types of fibers, Kuraray B-3 and Y-11, were used, which have 0.2-mm diameter and the double cladding structure. Their absorption and emission spectra are shown in Fig. 2.2. The blue and green lines are B-3 and Y-11, respectively. Positive and negative spectra represent the emission and absorption, respectively. In the primary test, fiber sheets with a size of 10×5 cm^2 were made using these fibers, and two layers of B-3 sheet were arranged on the top and two layers of Y-11 sheet at the bottom. The B-3 fiber has higher priority and was set on the top because the Cherenkov spectrum from the aerogel match as the B-3 absorption region and it emits photons with a short wavelength where the PMTs have a large quantum efficiency.

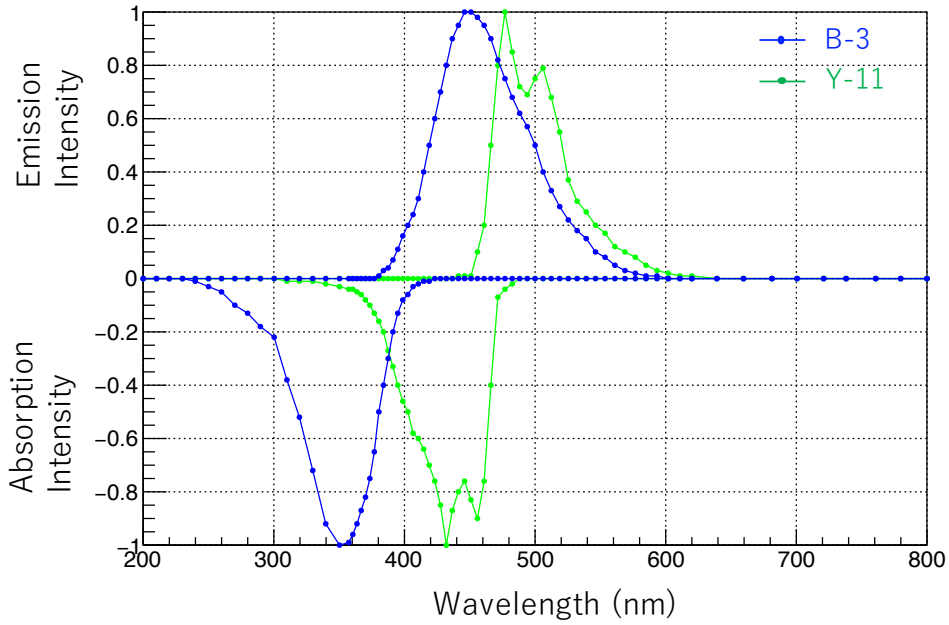

Fig. 2.2: The emission (up) and absorption (down) spectra of wavelength-shifting fiber B-3 and Y-11.

2.4 Photomultiplier tubes

In this study, Hamamatsu R9880U-210, H11934-200, and R1250-03 were used for PMTs. The efficiency depends on wavelength as shown in Fig. 2.3. R1250-03 with a bialkali photocathode (the red dots) has maximum quantum efficiency of 22% at 350–400 nm. The effective photo-cathode area has a 120-mm diameter. R9880U-210 and H11934-200 with an ultra bialkali photocathode (the black dots) have maximum quantum efficiency of 40% at 320–400 nm. The effective photo-cathode areas of R9880U-210 and H11934-200 are 8 mm in diameter and a square of 26.2 mm, respectively.

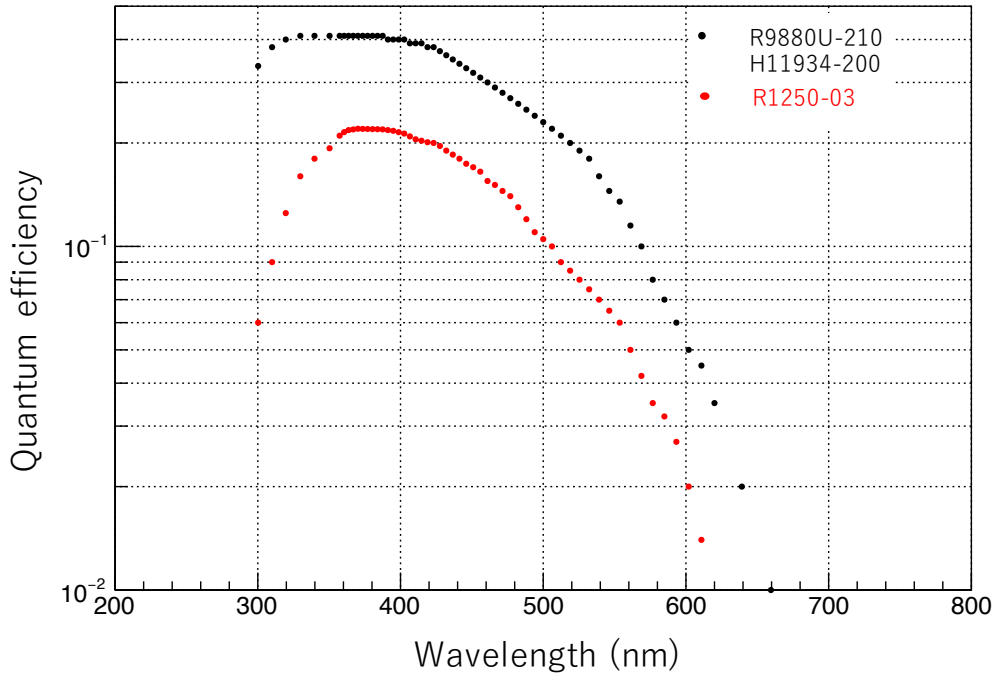

Fig. 2.3: PMT quantum efficiency of R1250-03 (red) and R9880U-210 and H11934-200 (black) as a function of the wavelength.

2.5 Measurement of light collection efficiency

I estimated the light collection efficiency of the wavelength-shifting fibers for Cherenkov photons by comparing experiment data and simulation calculations. In the experiment, cosmic-ray muons have an energy of a few GeV and the velocity close to the light velocity ($\beta \sim 1$). Thus, the yield of Cherenkov photons is large. In the simulation, I developed a spectra model (described above) and compared with the data.

A schematic view of the setup is shown in Fig. 2.4. A maximum of six tiles of aerogel with an average refractive index of 1.05 and a size of $100 \times 50 \times 10$ mm^3 were used in the test. Four trigger counters using plastic scintillators were put above and below the aerogel. A coincidence event of four signals implies a muon passing through the overlapping area of 50×30 mm^2.

The box in which the aerogel is mounted was attached to an inner reflection mirror made of aluminised Mylar film. The Cherenkov photons are guided to the outlet by a 45-degree reflector to downstream. The outlet size was 5×10 cm^2, on which (a) a 5-inch PMT (R1250-03) or (b) a wavelength-shifting fiber sheet with four PMTs (R9880U-210) were connected.

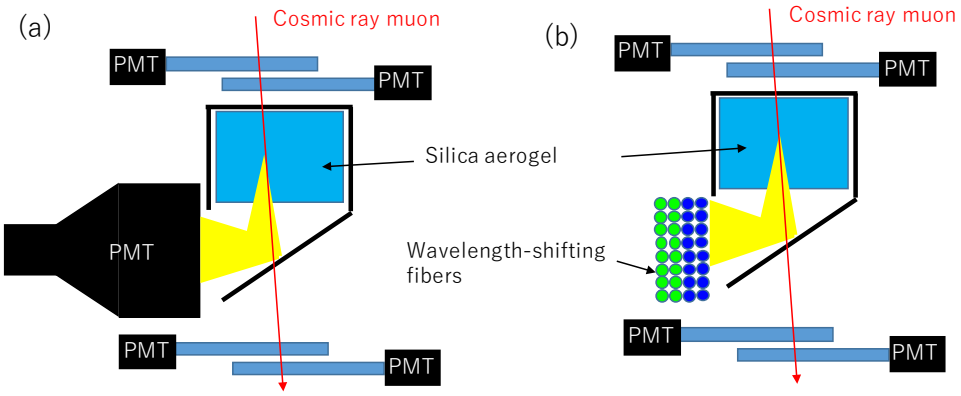

Fig. 2.4: Schematics of cosmic-ray test setup. (a) A direct PMT method and (b) wavelength-shifting fiber method.

Fig. 2.5 shows the distribution of the number of photoelectrons observed with the 5-inch PMT when cosmic-ray muons pass through the aerogel with a thickness of $D = 10$–60 mm. These histograms are consistent with the Poisson function $P(k, \nu) = e^{-\nu}\nu^k/k!$ expected for the pedestal peak. The mean

number of photoelectrons $\langle N_{p.e.} \rangle$ $(= \nu)$ was estimated by fitting. The pedestal events were approximately 17% of the total. It is considered that there are also processes not emitting Cherenkov photons in the coincidence events of four trigger counters, e.g., the events with two muons passing through both trigger counters at upstream and downstream simultaneously.

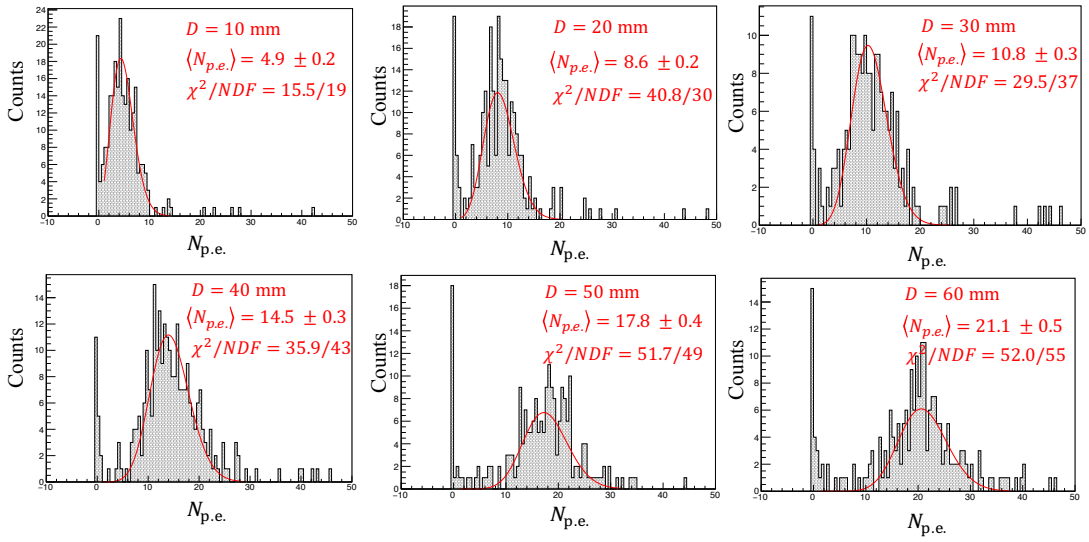

Fig. 2.5: Number of photoelectrons observed by the 5-inch PMT for the aerogel Cherenkov detector, when cosmic ray muons pass through the aerogel with difference thickness from D=10 to 60 mm.

The mean number $\langle N_{\mathrm{p.e.}} \rangle$ observed by fitting with a Poisson function is shown in Fig. 2.6 (left), which depends on the aerogel thickness D. The black dots are the data, the blue open circles are simulations, and the red line is the fitting function. The observed $\langle N_{\mathrm{p.e.}} \rangle$ tends to increase proportionally with D. In the simulation, the number of photoelectron $N_{\mathrm{p.e.}}$ observed with the PMT is given as

$$N_{\mathrm{p.e.}} = 2\pi\alpha \int d\lambda dL \frac{\varepsilon_{\mathrm{QE}}(\lambda) \cdot T(\lambda, L) \cdot \varepsilon_{\mathrm{ref}}}{\lambda^2} + N_0, \tag{2.4}$$

where L is the path length of the Cherenkov photon in the aerogel, λ is the wavelength, $\varepsilon_{\mathrm{QE}}(\lambda)$ is the quantum efficiency of the PMT used (R1250-03), $T(\lambda, L)$ is the transmittance in the aerogel which is transformed from

t to $L/\cos\theta_{\rm C}$ (see Eq. 2.3), $\varepsilon_{\rm ref}$ is the reflection factor, N_0 is the number of photoelectrons by Cherenkov radiation in the air, and the integral region is 200–800 nm. In order to be consistent with the data, $\varepsilon_{\rm ref}$ and N_0 were determined to be 0.466 ± 0.004 and 1.42 ± 0.03, respectively, with $\chi^2_{\rm min} = 30.7$ between the data and simulations. The observed number of photoelectrons is proportional to the thickness, and the slope is $(3.20 \pm 0.17) \times 10^{-1}$ mm^{-1}. The average detection efficiency is $83 \pm 2\%$ as shown in Fig. 2.6 (right).

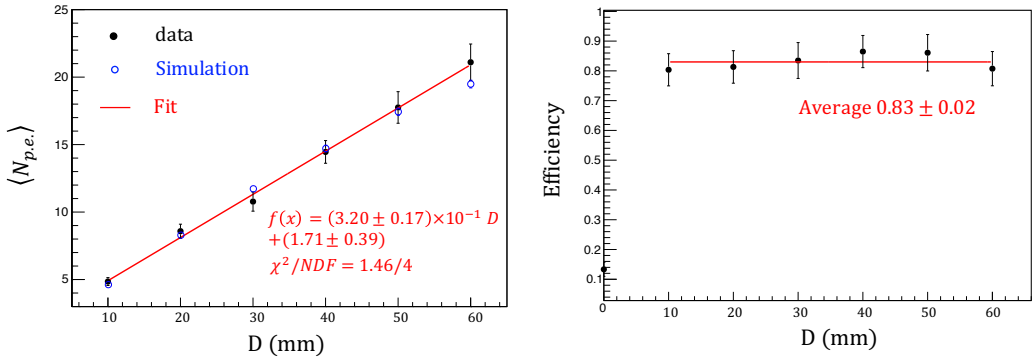

Fig. 2.6: Mean number of photoelectrons $\langle N_{\rm p.e.} \rangle$ (left) and the detection efficiency at the 0.5-p.e. threshold (right) depending on D.

In the method using wavelength-shifting fibers, both ends of the fibers were connected to four PMTs (R9880U-210) and red-shifted Cherenkov photons were observed by the PMTs. The distribution of $N^{(j)}_{\rm p.e.}$ observed by the PMTj is shown in Fig. 2.7, for $j = 1$–4 and aerogel thickness of $D = 60$ mm. The detection efficiencies of PMT1–4 at the 0.5-p.e. threshold are 0.26 ± 0.02, 0.23 ± 0.02, 0.09 ± 0.01, and 0.10 ± 0.01, respectively. The total numbers of photoelectrons $\sum_j N^{(j)}_{\rm p.e.}$ in the aerogel thickness $D = 10$–60 mm are shown in Fig. 2.8. The mean $N_{p.e.}$ was analyzed in the scheme of Poisson function $P(k, \nu)$ by regarding the inefficiency to be corresponding to $P(k = 0, \nu)$ which is just $\exp(-\nu)$. Since $\langle N_{\rm p.e.} \rangle = \nu$ in the Poisson distribution, the relation was obtained as

$$\langle N_{\rm p.e.} \rangle \equiv \nu = -ln(\text{inefficiency}). \tag{2.5}$$

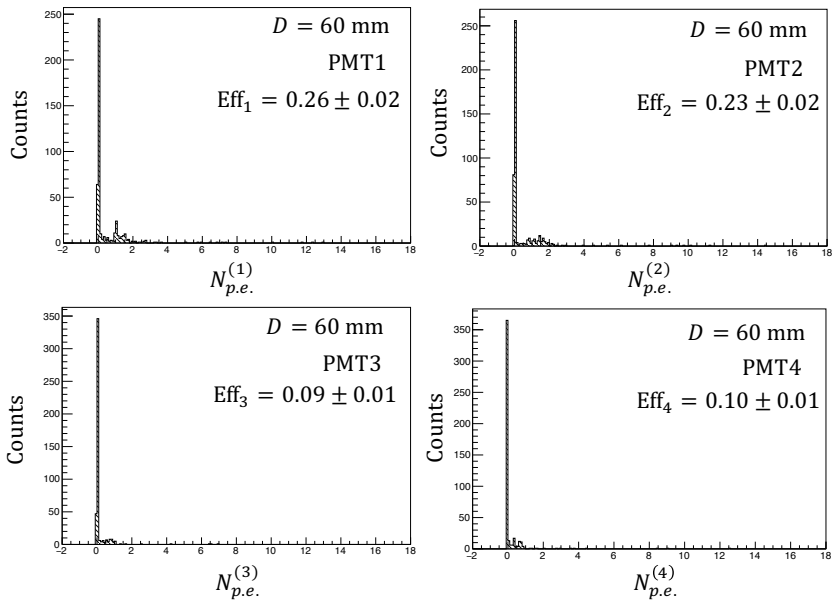

Fig. 2.7: Number of photoelectrons of PMT $j = 1$–4 in $D = 60$ mm.

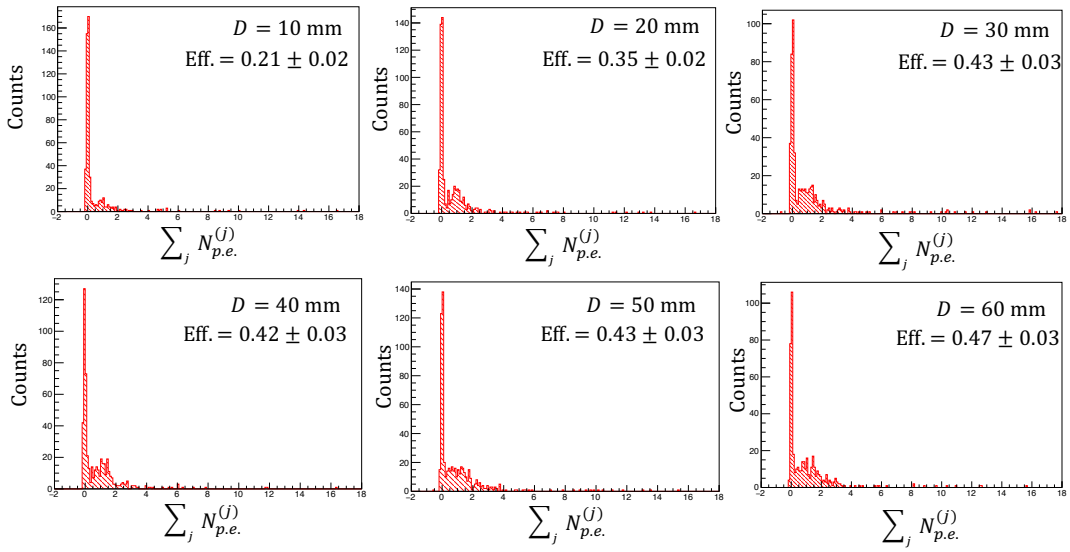

Fig. 2.8: The sum of $N^j_{\mathrm{p.e.}}$ in $D = 10$–60 mm.

Further, the pedestal events have accidental noise with the fraction of 17% same as in the method of direct PMT readout. The detection efficiency corrected for the efficiency/0.83 depends on the thickness D and is shown in Fig. 2.9 (left). The relation between $\langle N_{\rm p.e.}\rangle$ and D is also shown in Fig. 2.9 (right). The black dots are the data and the red line is the fitting function of $(0.85\pm0.11)(1-\exp\{-D/(27.2\pm6.5)\})+0.060\pm0.012$ with $\chi^2/{\rm NDF} = 3.92/4$. The blue open circles are the simulations. In the simulation, the absorption and re-emission factor in the wavelength-shifting fibers is unknown, thus the factor was determined by comparing $N_{\rm p.e.}$ with the data. The number of photoelectrons observed via the fibers is given as

$$\begin{aligned} N_{\rm p.e.} &= 2\pi\alpha \int d\lambda dL \frac{T(\lambda, L)\cdot\varepsilon_{\rm ref}}{\lambda^2} \\ &\Bigg\{ \quad g_{\rm core}^{\rm B-3}(\lambda,\lambda')\varepsilon_{\rm trap}\varepsilon_{\rm QE}(\lambda')d\lambda' \\ &+ \frac{1}{2} g_{\rm core}^{\rm B-3}(\lambda,\lambda') g_{\rm core}^{\rm Y-11}(\lambda',\lambda'')(1-\varepsilon_{\rm trap})\varepsilon_{\rm trap}\varepsilon_{\rm QE}(\lambda'')d\lambda'' \\ &+ (1-g_{\rm core}^{\rm B-3}) g_{\rm core}^{\rm Y-11}(\lambda,\lambda'')\varepsilon_{\rm trap}\varepsilon_{\rm QE}(\lambda'')d\lambda'' \Bigg\} \\ &+ N_0, \end{aligned} \tag{2.6}$$

where $\varepsilon_{\rm QE}(\lambda)$ is the quantum efficiency of the PMT (R9880U-210), $g_{\rm core}(\lambda,\lambda')$ is the absorption and re-emission factor in the core of wavelength-shifting fibers B-3 and Y-11, $\varepsilon_{\rm trap}$ is the trapping efficiency of 10.8%, and N_0 is the number of photoelectrons originated from Cherenkov radiation in the air observed via the fibers. This factor $g_{\rm core}(\lambda,\lambda')$ is the operator in the simulation to red-shift the wavelength from λ to λ' as shown Fig. 2.2 and it is assumed that the percentage of both factors is the same for B-3 and Y-11. In the curly brackets of Eq. 2.6, the first term represents the Cherenkov photons which meet the conditions to be absorbed in the B-3 fiber, red-shifted, re-emitted isotopically, satisfying the total reflection condition in the fiber, and then finally observed in the PMT. When the Cherenkov photon does not satisfy the total reflection condition in the B-3 fiber, it leaks out from the fiber and cannot be observed by the PMT. The second term denotes the leaking photon from the B-3 fiber but are absorbed by one of the Y-11 fibers under the the B-3 sheets, further red-shifted, and then observed. The acceptance factor is 1/2. The Cherenkov photon unabsorbed in a B-3 fiber enters the Y-11 fiber sheets. The third term represents the Cherenkov photons observed

in the PMT via the Y-11 fiber. The simulation was compared with the data in the region from $D = 10$ to 60 mm. In order to be consistent with the data, the free parameters were determined to be $g_{\rm core} = 0.435 \pm 0.003$ and $N_0 = 0.148 \pm 0.006$ with $\chi^2_{\rm min} = 6.6$.

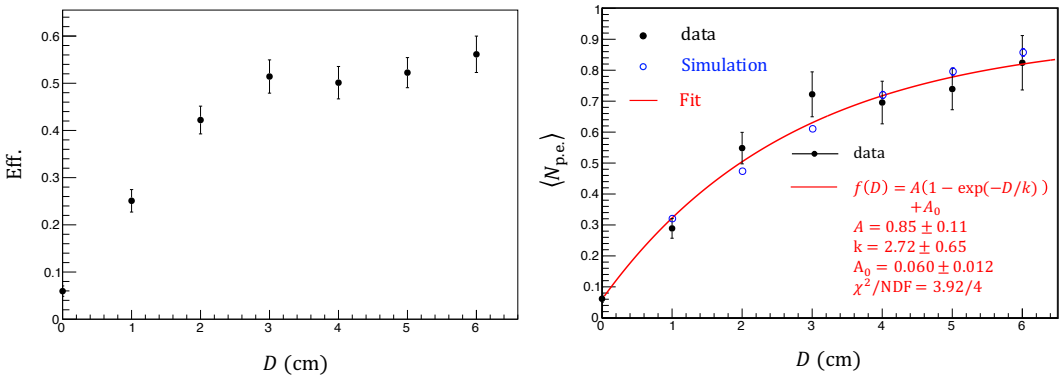

Fig. 2.9: The corrected detection efficiency (left) and mean number of photoelectrons $\langle N_{\rm p.e.}\rangle$ (right) depending on the aerogel thickness D.

As a result, the transmission characteristics of the Cherenkov photons from the silica aerogel to the PMT could be understood. An optical simulation model made the collection efficiency of the wavelength-shifting fibers clear, in particular, for the combination of B-3 and Y-11. Fig. 2.10 shows the simulation spectra of Cherenkov photons and photoelectrons originating from cosmic-ray muons in the aerogel with a thickness of 60 mm for both cases of direct PMT readout and via the wavelength shifting fibers. The black and cyan lines are the spectra of Cherenkov photons from the aerogel and those photons collected in the B-3 and Y-11 fibers, respectively. The yellow and red lines are the photoelectrons observed by the PMT directly and via the fibers, respectively. The blue, green, and magenta lines are, respectively, the photoelectrons from B-3, Y-11, and for the case of the photons which leaked into Y-11 from B-3.

The optical collection efficiency was defined as the ratio of the number of photons emitted from both ends of the fibers to the number of photons entering the side face of the fibers. The number of Cherenkov photons with shorter wavelength that reach the fibers tends to decrease depending on the aerogel thickness. Therefore, the collection efficiency increases depending

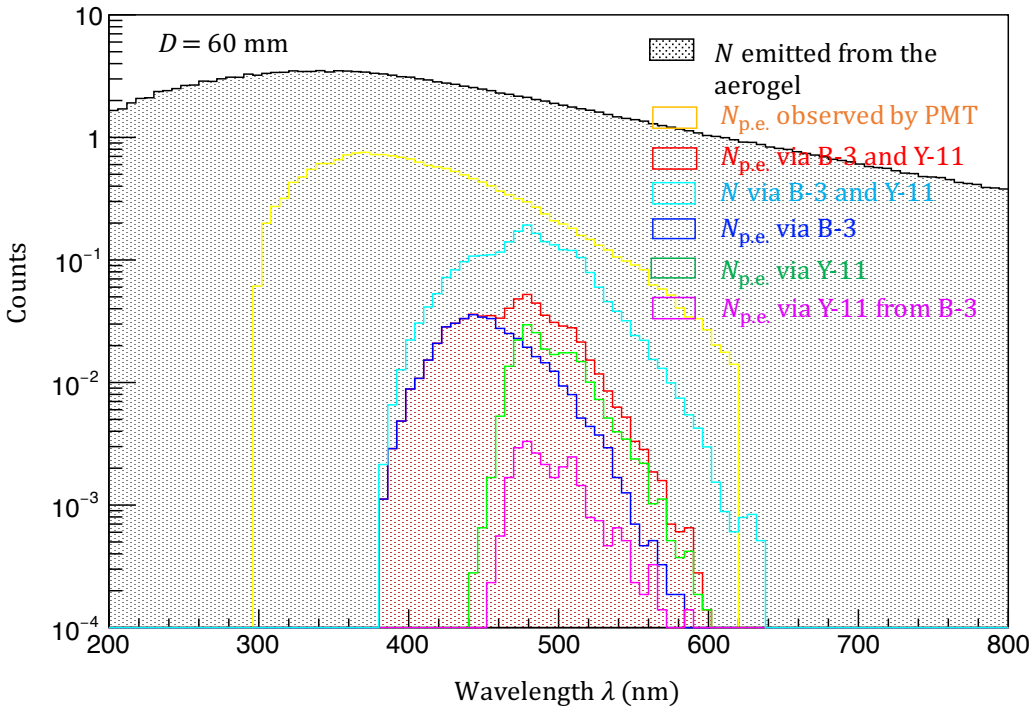

Fig. 2.10: Spectra of Cherenkov photons emitted from the aerogel (black), photoelectrons observed by PMT directly (yellow) and via the B-3 and Y-11 fibers (red), which is composed of B-3 (blue), Y-11 (green), and the leakage from B-3 to Y-11, and photons collected by B-3 and Y-11 fibers (cyan).

on the aerogel thickness as shown in Fig. 2.11, where the open circles are the simulation data and the red line is a fitting function of $(7.92 \pm 0.76) \times 10^{-3}(1-\exp(-D/(11.7\pm1.2)))+(5.78\pm0.80)\times10^{-3}$. The collection efficiency saturates at $1.37 \pm 0.15\%$.

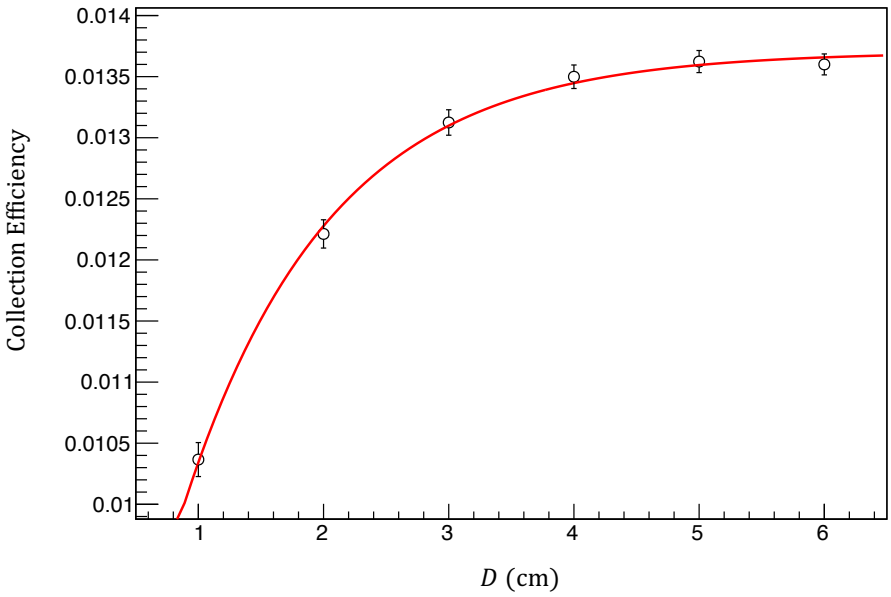

Fig. 2.11: Light collection efficiency versus the aerogel thickness D.

2.6 Impact of charged particles passing through the fibers

A test was performed to investigate the impact of a charged particle hitting the wavelength-shifting fibers using the setup as shown in Fig. 2.12 (left). Two layers of B-3 sheets were set on the top and two layers of Y-11 sheets on the bottom with optical shielding by black paper. Both ends of the B-3 and Y-11 fibers were connected to four PMTs (R9880U-210). Four scintillating detectors were put upstream and downstream of the Y-11 and B-3 fibers as the trigger counters. The number of photoelectrons is shown in Fig. 2.12 (right) when the cosmic-ray muon pass through the B-3 and Y-11 fibers. The blue histogram is the data. The red line is a fitting function of $AP(k/\alpha, \nu/\alpha)$, where A is the amplitude, $P(k, \nu)$ is the Poisson function, and α is a free parameter. As a result of fitting, $A = 80.6 \pm 4.8$, $\nu = 5.71 \pm 0.09$, and $\alpha = 2.18 \pm 0.13$ were obtained with $\chi^2/\mathrm{NDF} = 222/184$. Therefore, the mean number of photoelectrons of 5.71 ± 0.09 and the detection efficiency of $98.0 \pm 2.0\%$ at the 0.5-p.e. threshold were obtained in the test.

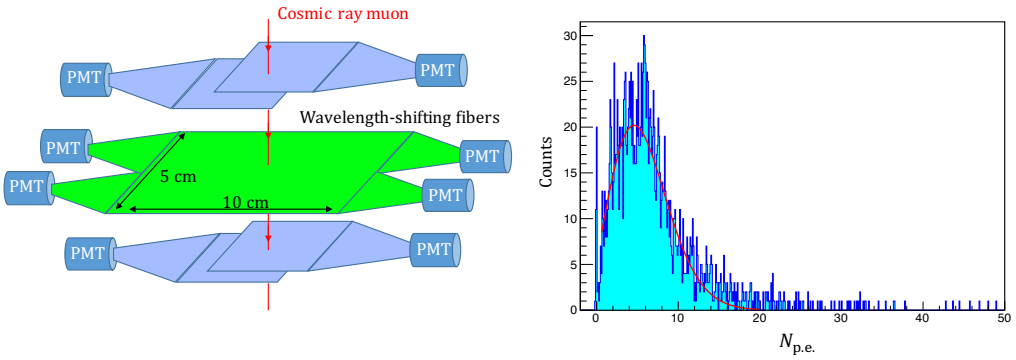

Fig. 2.12: Setup (left) and distribution of photoelectrons (right).

It is assumed that the Cherenkov photons are emitted in the fibers when the cosmic-ray muon passes through the fibers. The fiber has a 0.2-mm diameter, a refractive index of 1.59, and a density of 1.06 g/cm^3 in the core. A sheet consists of four layers. In the simulation, an average 82.7 Cherenkov photons were emitted from the fibers and it was predicted that $\langle N_{\mathrm{p.e.}} \rangle = 0.17$ should be observed by the PMTs connected to both ends of the fibers. Therefore, this data is not consistent with the simulation calculation.

It was found that the wavelength-shifting fibers emit photons by different principles from Cherenkov radiation when a charged particle passes through the fiber. It is considered that the wavelength shifter in the fiber has an emission property similar to the scintillation radiation.

2.7 Cherenkov photons from ^{90}Sr and ^{90}Y β rays

I estimated the number of Cherenkov photons from ^{90}Sr and ^{90}Y β rays and the photoelectrons observed in the PMT using the simulation model prepared above.

The energy spectrum of ^{90}Sr and ^{90}Y β rays has a continuous distribution as shown in Fig. 1.1. The β rays lose energy in the silica aerogel passing through there, and eventually they do not satisfy the Cherenkov condition, e.g., 2.28-MeV β ray which passed through the aerogel of 8-mm length or more becomes $K < 1.31$ MeV and emits no Cherenkov photons. It was calculated that the 2.28-MeV β ray emits a total of approximately 16 photons in the aerogel. The relation between $K_{\rm max}$ and the number of Cherenkov photons N in the simulation is shown in Fig. 2.13 (left). The percentage distribution of N emitted by ^{90}Sr and ^{90}Y β rays depends on the β-ray energy spectrum as shown in Fig. 2.13 (right).

A test was performed in order to observe Cherenkov photons from the aerogel by ^{90}Y β rays. The wavelength-shifting fiber light guide was set to the downstream of three layers of the aerogel tiles with $n = 1.041$. A trigger counter sheet made of a scintillating fiber with 0.2-mm diameter was set to the upstream of the aerogel and a 23.6 kBq ^{90}Sr source was put on the upstream of the trigger counter, namely the photoelectrons of the PMTs connected to the fibers were measured when a ^{90}Y β ray passes through the trigger counter. A black sheet was put between the aerogel and the fibers for optical shielding. The events with Cherenkov photons from the aerogel were observed by comparison of the data with and without the optical shielding. Fig. 2.14 (left) shows the distribution of photoelectrons with (magenta) and without the optical shielding (black). The peak at 6–8 p.e. suggests events which emit photons when the β rays enter the fibers. The difference of these distribution is shown in Fig. 2.14 (right). The red line is a fitting function which has a Gaussian function for the pedestal and also a Poisson

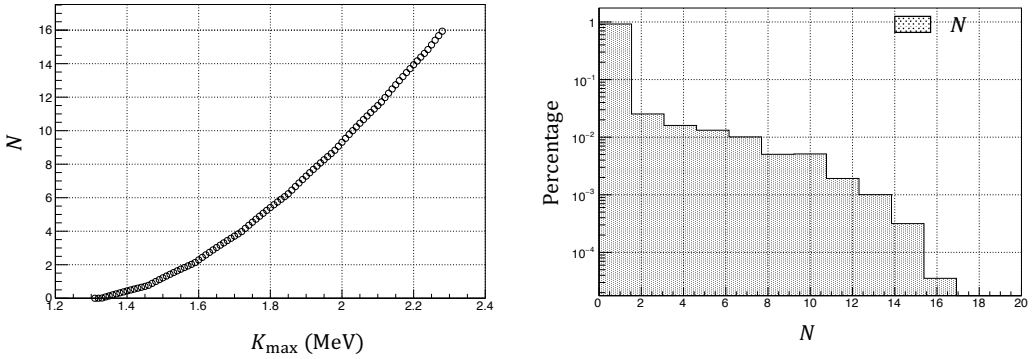

Fig. 2.13: Relation between β-ray energy $K_{\max}$ and the number of emitted Cherenkov photons N in the silica aerogel with $n = 1.041$ (left) and percentage distribution of the number of Cherenkov photons N from the silica aerogel by ^{90}Sr and ^{90}Y β rays (right).

function. For the Gaussian function, a mean value of 0.00 ± 0.10 and a standard deviation of 0.10 ± 0.02 were determined, and for the Poisson function, $\nu = 0.72 \pm 0.13$ and $\alpha = 0.24 \pm 0.12$ were determined with $\chi^2/\mathrm{NDF} = 66.3/33$ for the combined functions.

As a result of integration of the fitted Poisson function, the Cherenkov photons from the aerogel by ^{90}Y β rays could be observed to be 2.4 ± 1.3 s^{-1} using the wavelength-shifting fibers. This result was consistent with a predicted count rate of 2.35 s^{-1} by the simulation calculation, when the radioactivity of ^{90}Sr source is 23.6 kBq, the experimental acceptance is 9.9%, and the calculated efficiency is 5.04×10^{-4} for ^{90}Sr and ^{90}Y. This efficiency was calculated from (1) the coefficient of 1.84×10^{-3} from N to $\langle N_{\mathrm{p.e.}} \rangle$ observed by the PMT via B-3 and Y-11 fibers and (2) the relation between the detection efficiency and $\langle N_{\mathrm{p.e.}} \rangle$ (see Eq. 2.5).

2.8 Accidental noise by ^{137}Cs γ rays

I investigated the responses to accidental γ rays in the cases of direct PMT readout and via the wavelength-shifting fibers. It is known that ^{137}Cs emits a 662-keV γ ray 2.55 ms after the β decay with a branching ratio of 94.4% [4].

In a setup, a 5-inch PMT (R1250-03) or the fiber light guide of B-3

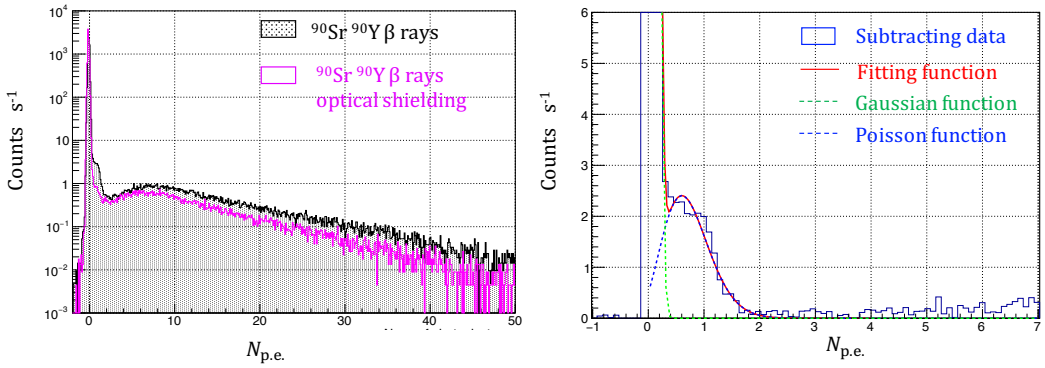

Fig. 2.14: Distribution of photoelectrons with and without the optical shielding using the wavelength-shifting fibers (left) and the difference of these data (right).

and Y-11 were set on the downstream of the trigger counter and a ^{137}Cs source was put on the upstream of the trigger counter. The distribution of photoelectrons is shown in Fig. 2.15. The black and red are, respectively, the data in the case of the 5-inch PMT readout and of the fiber light guide. The detection efficiency with 0.5-p.e. threshold for the direct PMT and fiber readout were 0.91±0.02% and 0.10±0.01%. The ratio of efficiencies for direct PMT reading to that for fibers reading was 11.0 ± 1.1% and was defined as the accidental noise ratio.

When the γ rays hit the entrance window and photocathode of the PMT, noise signals are produced. In the entrance window, electrons which are knocked out by the γ rays emit Cherenkov photons. In the photo-cathode, knocked out electrons produce noise signals directly. When the γ rays hit the fiber, knocked out electrons can emit photons in the fibers.

The probability of γ-ray interaction depends on the amount of substance. The entrance window of PMT has a density of 2.6 g/cm^3 and a thickness of 2–3 mm. The fiber light guide has a density of 1.06 g/cm^3 and a thickness of 0.8 mm. The material ratio of the fiber to the entrance window of 11–16% corresponds to the ratio of the probability for γ rays and can explained the experimental accidental noise ratio. Therefore, it was demonstrated that the method of fiber light guide can suppress the accidental γ rays more effectively than the direct PMT method.

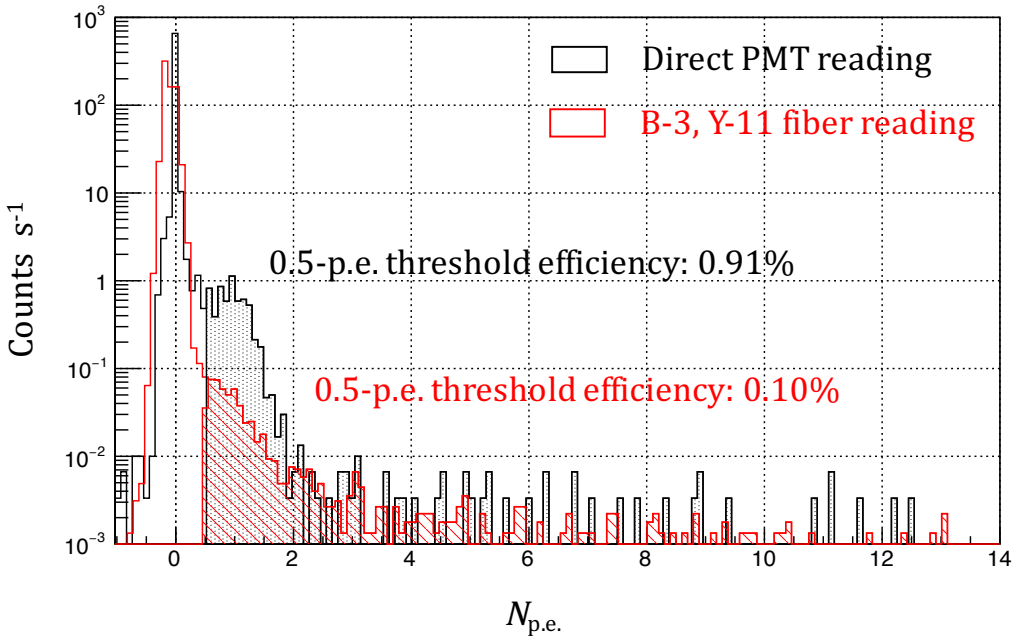

Fig. 2.15: Distribution of photoelectrons for ^{137}Cs γ rays in direct PMT readout (black) and B-3 and Y-11 fibers readout (red) for those events with $N_{\text{p.e.}} > 0.5$ (black and red hatched areas).

2.9 Result

A model which explains the light transmittance in the aerogel, the spectra of Cherenkov photons, absorption and re-emission of the wavelength-shifting fibers was developed for the simulation in order to reproduce the experimental data using cosmic-ray muons. The optical collection efficiency of the B-3 and Y-11 fibers for Cherenkov photons was estimated to be 1.0–1.4% using these models. When the cosmic-ray muons pass through the fibers, a number of photoelectrons which cannot be explained by Cherenkov radiation in the fibers was observed. It was found that the wavelength-shifting fiber also has a property similar to scintillation radiation. It was calculated that a maximum of 16 Cherenkov photons are emitted from a ^{90}Y β rays in the silica aerogel with $n = 1.041$. The Cherenkov photons originating from ^{90}Y β rays via the fiber light guide were observed, and the data was consistent with the simulation calculation. It was demonstrated that the method using the wavelength-shifting fibers can suppress accidental γ rays more effectively

in comparison with the method of direct PMT read-out. For an actual β-ray sample inspection, it is required to extend the effective area. In this case also the method of fiber light guide can suppress the noise increase due to the extension of the effective area.

Chapter 3

Background study of environmental radiation

In the measurement of a few Bq ^{90}Sr radioactivity, the environmental radiation can become the background noise. At first, since the cosmic-ray muon is known well, this is described succinctly in this Chapter. There are ^{238}U and ^{232}Th in building concrete and the γ rays with $E_\gamma > 2$ MeV from ^{214}Bi and ^{208}Tl as the progenies can be observed. After ^{222}Rn decays in the air, the radon progenies may fall on the sample surface. It is possible that the β ray from ^{214}Bi as the progenies with $K_{\max} = 3.27$ MeV become uback-ground noise. Furthermore, the air may contain ^{214}Bi. In this Chapter, the influence of the background noise on detector performance are investigated.

3.1 Cosmic-ray muons

Cosmic-ray muons pass through the detector in this background study and emit Cherenkov photons in the silica aerogel since the velocity is close to the light velocity. Cosmic-ray veto counters made of plastic scintillators were set on four sides of the Cherenkov detector as well as over the detector because the cosmic-ray muons come not only from the top of the zenith angle but also from the side. The veto counters are required to have a detection efficiency of more than 99.9% for cosmic-ray muons.

3.2 γ-rays energy spectroscopy of the air

It is known that there is ^{222}Rn in the air, which is one of the progenies in the ^{238}U decay chain. The half life is 3.8 days. It emits alpha rays of 5.49 MeV [4]. The average annual radiative dose is estimated as 1.15 mSv for the radon inhalation with the mean concentration of 45 Bq/m^3 in the air [20]. Bismuth-214, as one of the ^{222}Rn progenies, emits beta rays with a maximum energy of 3.27 MeV, which satisfies the Cherenkov condition. Thus, the estimate of the radioactive dose has to take into account this contribution, if ^{214}Bi stays in the air.

3.2.1 Setup

The energy spectrum of gamma rays originating from the radioactive isotopes in the air was measured indoors and outdoors. The experimental setup in the case of outdoors is shown in Fig. 3.1.

A BGO ($Bi_4Ge_3O_{12}$) scintillator with a size of 50-mm diameter, 50-mm depth, and density of 7.10 g/cm^3 was used as the detector. Teflon sheets were attached to the top and side faces as diffuse reflectors, and the bottom surface was connected to a PMT (Hamamatsu R6231) with optical grease.

In order to suppress the cosmic-ray muon background three veto counters were placed on the top, front, and back sides of the BGO crystal. Each one of the veto counters consisted of a plastic scintillator with a size of $200 \times 100 \times 5$ mm^3 and a PMT (Hamamatsu H1161) was connected on both ends via light guides made of Acryl.

Twenty four layers of lead plates with the size of $990 \times 392 \times 4$ mm^3 (96-mm thick) were set under these detectors in order to suppress the background gamma rays from the surrounding concrete structure. Brass blocks with a thickness of more than 50 mm were also used as the top and side shielding.

3.2.2 Monte Carlo simulation

For comparison with the results of the tests, the energy spectra of gamma rays emitted from radionuclides ^{214}Bi, ^{208}Tl, and ^{40}K in the BGO detector were calculated with a Monte Carlo (MC) simulation code of GEANT4, in which the energy resolution σ_E depending on E was considered. In the box of the radiative shield with brass and lead blocks, the background from the

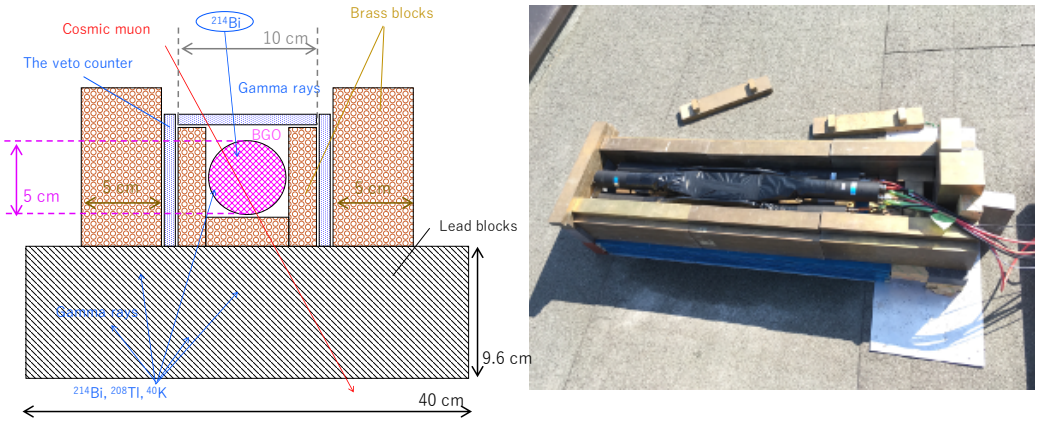

Fig. 3.1: Setup of the BGO detector on the roof of the building. A schematic of cross section (left) and a picture of the setup on the roof (right).

external gamma rays can be estimated. The results are shown in Fig. 3.2 together with experimental data.

3.2.3 Results

The measured energy spectra indoors and outdoors are shown in Fig. 3.2. The red and blue solid lines are the experimental data indoors and outdoors on the roof, respectively. The energy flux above 3 MeV that were observed commonly indoors and outdoors is understood to be bremsstrahlung γ rays from cosmic-ray muons mainly. The red dashed line presents the flux of the bremsstrahlung γ rays. The green, magenta, and cyan dashed lines are the MC-calculated yields for ^{214}Bi, ^{40}K, and ^{208}Tl, respectively, assuming a concentration of 1 Bq/m^3 in the air. The black line is the subtraction of the neutral cosmic rays from the data indoors. As a result, the peaks from ^{214}Bi, ^{40}K, and ^{208}Tl were observed at 1,720 keV, 1,462 keV, and 2,600 keV, respectively, indoors, however these peaks were not observed outdoor on the roof. The reason is considered to be the fact that there is a concrete ceiling which contains ^{214}Bi, ^{40}K, and ^{208}Tl over the detector indoor but not outdoor.

It was found that the noise of gamma rays from concrete and cosmic ray γ shower (consistent with ref. [21]) is dominant for the observation of γ rays emitted from ^{214}Bi in the air. For the 1,720-keV peak observation, the detection limit of ^{214}Bi concentration is estimated to be 100 Bq/m^3 in

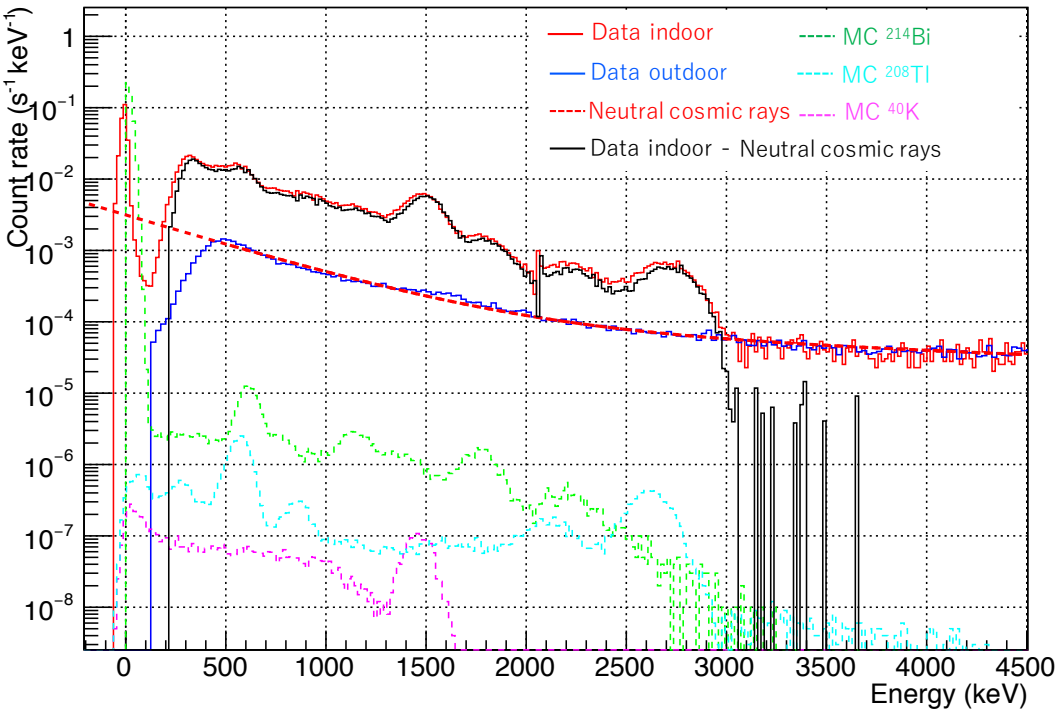

Fig. 3.2: Measured BGO energy spectra indoor (red) and on the roof (blue) and the expanded spectrum corrected for cosmic ray background (black). Expected yield of ^{214}Bi, ^{40}K, and ^{208}Tl with 1 Bq/m^3 in the air are also shown.

the air by suppressing the background events from cosmic ray muons and gamma rays emitted from the concrete. The radon concentration in the air was measured to be 4–184 Bq/m^3 all over the world [20].

Although the ^{214}Bi radioactivity was not observed this time, its upper limit was determined to be 100 Bq/m^3 in the air in the presence of neutral cosmic ray background. This level of background from ^{214}Bi in the air is negligible to measure ^{90}Sr concentration in the detector with air volume of 5–10 L because the ^{214}Bi concentration corresponds to approximately 0.5–1 Bq in the sample.

In this study, the accidental noise was due to the events of γ rays with $E_\gamma > 2$ MeV emitted from ^{214}Bi and ^{208}Tl in concrete blocks rather than that from ^{214}Bi in the air. Thus, the detector should be shielded externally. However, it is not easy to suppress most of these events with the consequence that high energy neutral cosmic rays sets a limit in the measurement.

3.3 β-rays surface inspection of sample sheets adsorbing radon progenies

3.3.1 Setup

The setup is shown in Fig. 3.3. The β rays emitted from the hermetically-sealed air inside the box were measured using a β-ray counter based on scintillating fibers (Fig. 3.4) with a veto counter system for suppressing cosmic-muon events. These counters were covered by lead blocks with a thickness of 32 mm for the suppression of external gamma rays from ^{214}Bi, ^{208}Tl, and ^{40}K in the concrete. With this thickness, 85% of these backgrounds could be suppressed at $E_\gamma = 2$ MeV.

The detector used scintillating fibers (Kuraray SCSF-78MJ), and PMTs (Hamamatsu R9880U-210) on both ends. The effective area of the scintillating fibers was 30×10 cm^2 (see Fig. 3.3.).

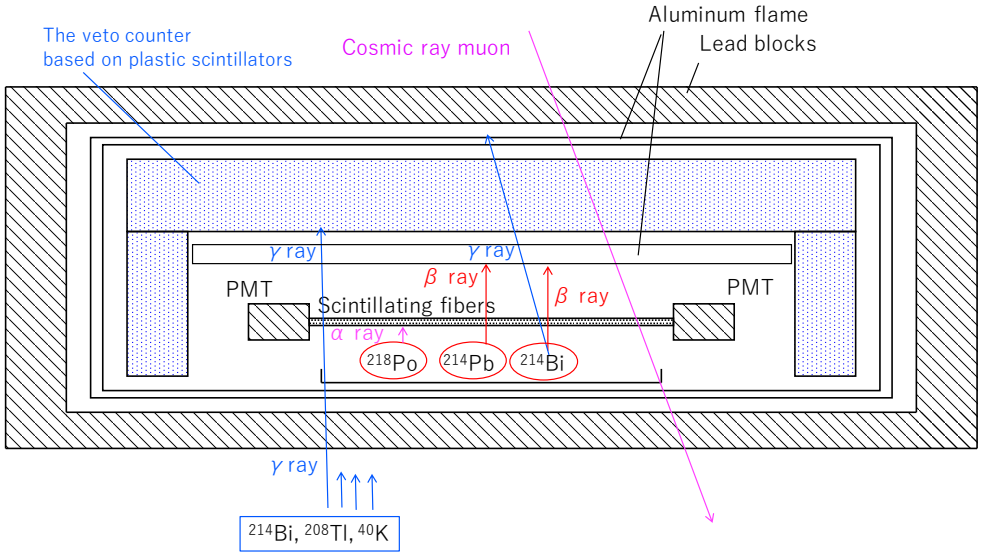

Fig. 3.3: Setup for the β ray measurement. A schematic cross section of the detector.

Fig. 3.4: The β-ray counter based on scintillating fibers with an effective area of 30×10 cm.

3.3.2 Detection efficiency

A ^{90}Sr source with 23.6 kBq was set under the β-ray counter for the estimation of the detection efficiency. The event rate N_{Sr} was $(2.049 \pm 0.002) \times 10^7$ h^{-1}. The detection efficiency was deduced to be $(8.68 \pm 0.01) \times 10^2$ Bq^{-1} h^{-1} by calculating $(N_{\mathrm{Sr}} - N_{\mathrm{BG}})/A_{\mathrm{Sr}}T$, where N_{BG} is the number of background event without the source, A_{Sr} is the radioactivity of the source, and T is the measuring time. N_{BG} was measured in advance to be $(3.67 \pm 0.14) \times 10^3$ h^{-1}, where the error represents the standard deviation of 60 measurements.

3.3.3 Sample

The sample sheets used were made of 11-μm thick polyethylene with a size of 30×10 cm^2 and a density of 1.4 g/cm^3. The samples were placed on an aluminium plate connected to the earth in a windless room for a few hours before being inspected because the adsorption effect is dependent on the static electricity. In brief, the adsorption effect of natural drops of radon progenies on the sample surface was measured. In order to gain the radon progenies yield in the measurement, ten layers of sheets were set in the detector.

3.3.4 Monte Carlo simulation

In the β-ray inspection, a difference occurred in the detection efficiency between the β rays emitted from the top surface and inside of the stacked sample sheets. The correction coefficient for this difference in each sheet was calculated by MC simulation calculation.

3.3.5 Time spectra of count rate

The measured time spectrum of the polyethylene sheets which were exposed for 4 h 40 min in the roomair is shown in Fig. 3.5. The black dots are data, the red curve is the fitting for three radioisotopes in the chain ^{218}Po $\rightarrow^{214}$ Pb $\rightarrow^{214}$ Bi, the green dashed line is the background rate, and the blue dashed line is a simple exponential function of $(3.22 \pm 0.04)\exp(-t/ln2\ \tau_{1/2}) + 1.02 \pm 0.01$ with $\tau_{1/2} = (0.95 \pm 0.02)$ h and with a fit quality with $\chi^2/\mathrm{NDF} = 0.32/69$. The red function is given as

$$\begin{aligned} f(t) \quad &= \frac{\lambda_1\lambda_2 x_0^{(1)}}{(\lambda_1-\lambda_2)(\lambda_1-\lambda_3)}\exp(-\lambda_1 t) \\ &+ \left(\frac{\lambda_1\lambda_2 x_0^{(1)}}{(\lambda_2-\lambda_1)(\lambda_2-\lambda_3)} + \frac{\lambda_2 x_0^{(2)}}{\lambda_3-\lambda_2}\right)\exp(-\lambda_2 t) \\ &+ \left(\frac{\lambda_1\lambda_2 x_0^{(1)}}{(\lambda_2-\lambda_1)(\lambda_2-\lambda_3)} + \frac{\lambda_2 x_0^{(2)}}{\lambda_3-\lambda_2} + x_0^{(3)}\right)\exp(-\lambda_3 t) \\ &+ R_{BG}, \end{aligned} \tag{3.1}$$

where $\lambda_j = 1/ln2\ \tau_{1/2}^{(j)}$, $x_0{}^{(j)}$ is the initial intensity of count rate for each radon progeny, and $j = 1$, 2, and 3 represent ^{218}Po, ^{214}Pb, and ^{214}Bi, respectively. $\tau_{1/2}^{(j)}$ are half lives of ^{218}Po (3.1 min), ^{214}Pb (26.8 min), and ^{214}Bi (19.9 min), respectively.

3.3.6 Radioactivity concentration

The concentration of radioactivity in the sample A is given as

$$A = \sum_j \left(C(t_j) - R_{\mathrm{BG}}\right)\Delta t_j \frac{\eta_\varepsilon k_\rho}{\varepsilon_{\mathrm{Sr}} S}, \tag{3.2}$$

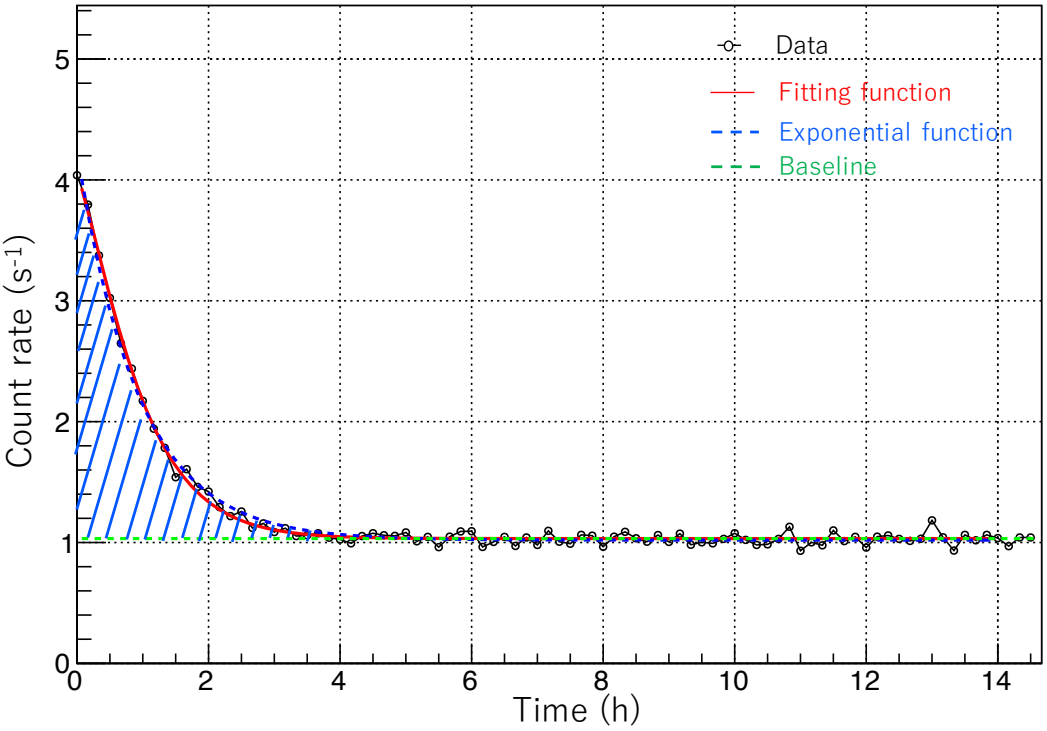

Fig. 3.5: Result of the β-rays inspection. The time spectrum of count rates for the polyethylene sample which is exposed for 4 h 40 min in the roomair.

where $C(t_j)$ and R_{BG} are the counting number of signal and background for 10 min, Δt is 10 min, $\varepsilon_{\mathrm{Sr}}$ is the estimated detection efficiency for ^{90}Sr, $\eta_\varepsilon = 0.37$ is the ratio of the ^{90}Sr efficiency to that for the radon progenies, k_ρ is the correction coefficient, and S is the effective area of 30×10 cm^2. η_ε was estimated by calculating the detection efficiency for these radionuclides in a MC simulation calculation. $k_\rho = 1.15$ is the correction for the difference between the inner layers and top layers in the polyethylene sheet. As a result, this polyethylene sample sheet had the concentration of contamination of (17.9$\pm$5.8) Bq/m^2 in a layer, where the error contains the standard deviation of background rate, a fluctuation of the counting error, and the uncertainty of counts due to dead time between the sample set and start time.

3.3.7 Impact of exposure time in the air

The relation between the exposure time in the air and the radioactivity concentration on the polyethylene sheet is shown in Fig. 3.6. Open cir-

cles are data and the red curve is the fitting function of $(17.9 \pm 0.5)\{1 - \exp(-(t/(1.68 \pm 0.06)\ \mathrm{h}))\}$ with the exposure time t with $\chi^2/\mathrm{NDF} = 631/11$. As a result, it was observed that the amount of radioactive concentration related to radon progenies exponentially is depending on the period that the sample was exposed in the air.

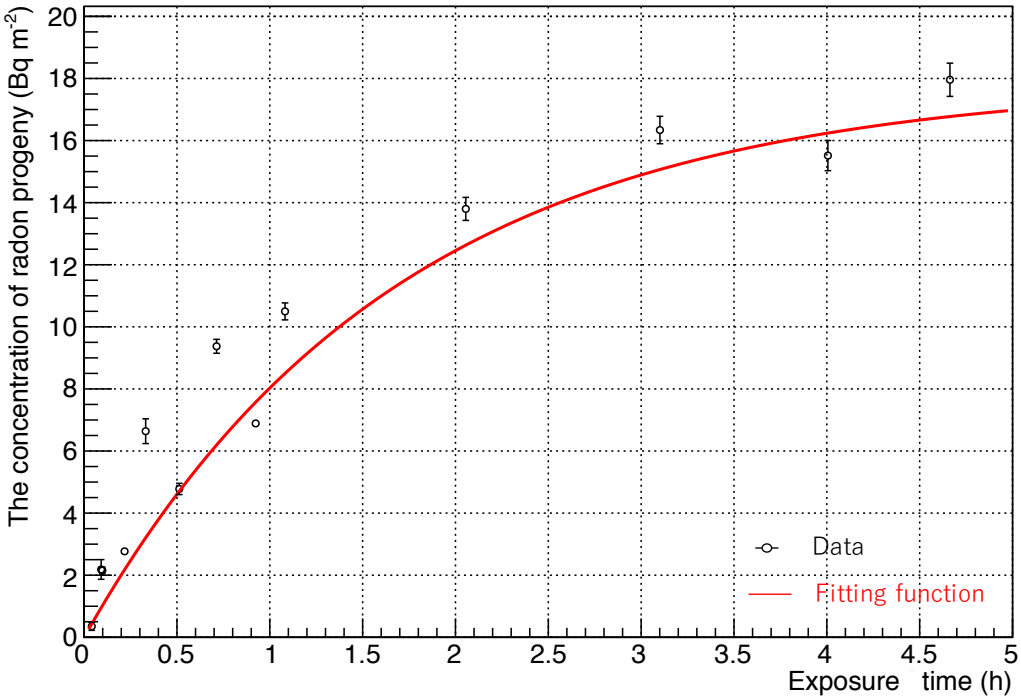

Fig. 3.6: The relation between the exposure time in the air and the radioactivity concentration on the polyethylene sheet.

3.3.8 Decay time constant

In the count rate result, the half life was determined by a simple exponential fitting. This indicates a fluctuation of the ratio of radon progenies (^{218}Po, ^{214}Pb, and ^{214}Bi) on the sample sheet just before inspection. Figure 3.7 shows the relation between the time constant (half life) and the exposure time. The open circles are data. The red lines represent the average half life and standard deviation when the sample was exposed over one hour; the time constant was observed to be (39.5 ± 2.2) min. Therefore, the ratio of radon progenies in the sample becomes constant.

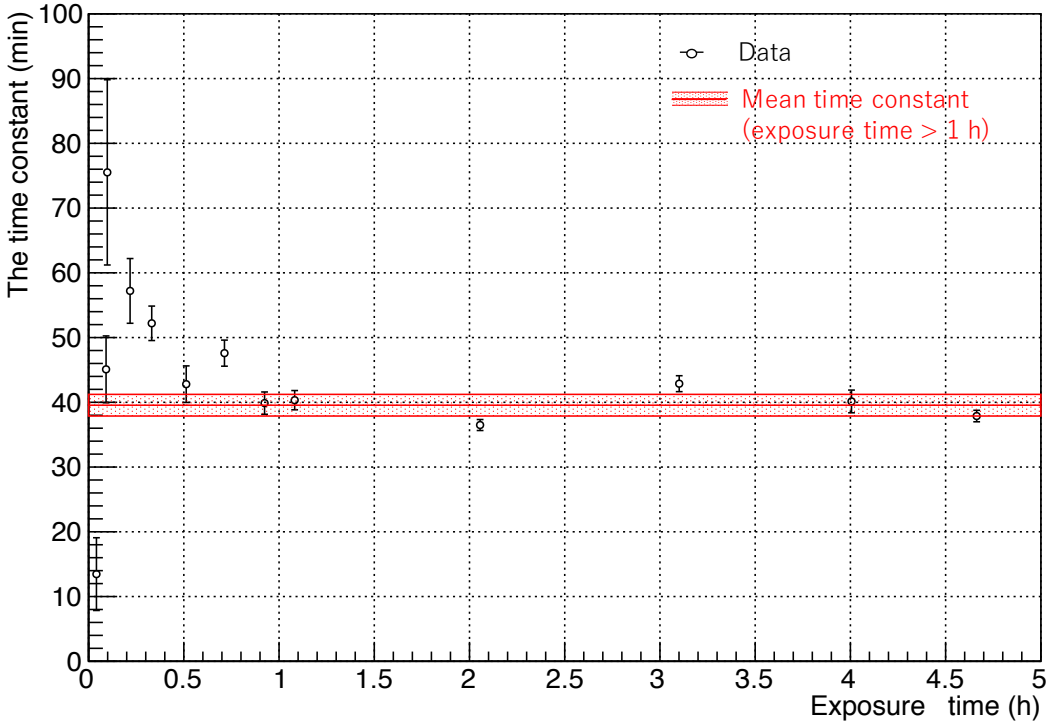

Fig. 3.7: Result of the β-rays inspection. The time fluctuation of count rates for the polyethylene sample.

3.3.9 The ratio of radon progenies on the sample

The free parameters $x_0^{(1)}$, $x_0^{(2)}$, and $x_0^{(3)}$ in Eq. 3.1 are, respectively, the initial intensity of count rate for ^{218}Po, ^{214}Pb, and ^{214}Bi. It is implied that the ratio of $x_0^{(1)} : x_0^{(2)} : x_0^{(3)}$ is the concentration ratio of ^{218}Po:^{214}Pb:^{214}Bi attached to the sample just before inspection. The relation between the ratio and the exposure time for the sample put on an Al plate is shown in Fig. 3.8. The black, red, and blue dots are the ratio of radon progenies ^{218}Po, ^{214}Pb, and ^{214}Bi, respectively. The reason why the error for $t < 1$ h is large is statistics due to small concentration of radioactivity on the sample. The ratio of ^{218}Po just after the exposure shows a significant existence of ^{218}Po on the sample, while those of ^{214}Pb and ^{214}Bi are dominant after one hour.

Here, a scenario is considered that only ^{218}Po falls on the sample just after the radon decays in the air, namely there is no radon progenies in the air. The black, red, and blue solid lines are the behaviour of ^{218}Po, ^{214}Pb, and ^{214}Bi on the sample in this scenario as shown in Fig. 3.8, respectively. This

result suggests that we should reject the scenario clearly that ^{218}Po is only falling. Because, the ^{218}Po, ^{214}Pb, and ^{214}Bi should be in the radioactive equilibrium condition only if ^{218}Po is adsorbed and decays on the sample. Therefore, it is suggested that there are not only ^{218}Po but also ^{214}Pb and ^{214}Bi in the air. The best fit scenario for exposure time $t > 1$ h is showed as the dashed lines in Fig. 3.8, where the ratio is ^{218}Po:^{214}Pb:^{214}Bi=3:30:5.

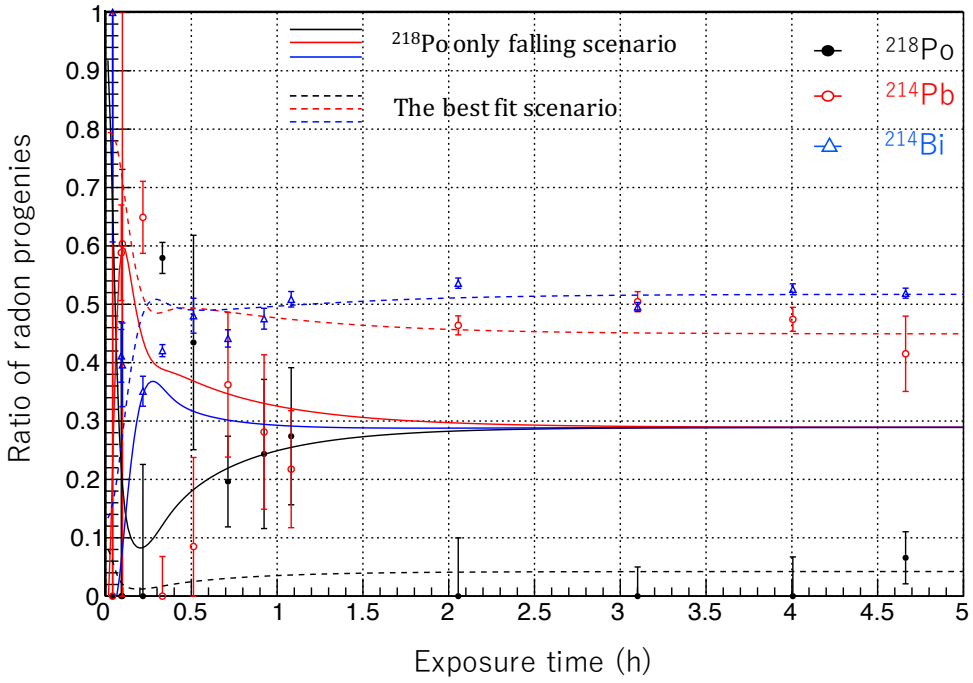

Fig. 3.8: The relation between the ratio and the exposure time for polyethylene samples.

3.3.10 Result

As a result, it was found that the radon progenies of (17.9 ± 0.5) Bq/m^2 were attached to the sample sheets. It is not negligible to inspect with a large effective area, thus the sample should be not exposed to the air. It is suggested Indirectly that there are the radon progenies in the air. This suggestion could be a clue for a search for reason of lung cancer occurring in non-smokers by attributing in to the exposures to the radon progenies by inhalation.

Chapter 4

Design of a prototype detector

I produced a prototype detector after some prototyping [22–24]. The cross section of this detector is shown in Fig. 4.1, which is composed of (1) a threshold-type aerogel Cherenkov detector using wavelength-shifting fibers, (2) a trigger counter using scintillating fibers, and (3) cosmic-ray veto counters using plastic scintillators and wavelength-shifting fibers. In addition, it is shielded using lead and brass blocks to suppress the background noise originated from environmental radiation. In this section, the specification of each component of this prototype detector is described in detail.

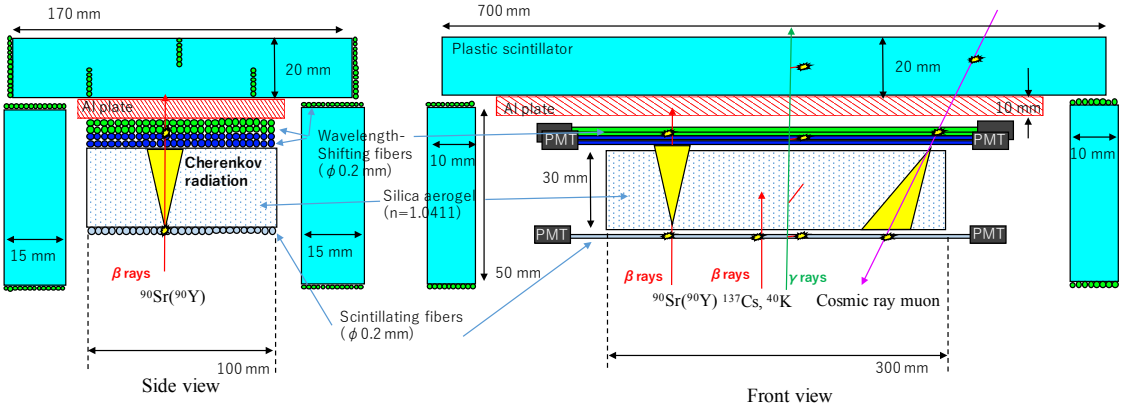

Fig. 4.1: Structure of the prototype detector. Side view (left) and front view (right) of the cross sections.

4.1 Threshold-type Cherenkov counter

The threshold-type aerogel Cherenkov counter is characterised by the application of two kinds of wavelength-shifting fibers (Kuraray B-3 and Y-11) with different absorption-wavelength regions.

It has nine tiles of silica aerogel ($96\times96\times10$ mm^3) with a mean refractive index of 1.0411, density of 0.15 g/cm^3, and the transmission length of 40.8 mm at 400-nm wavelength. The properties of these silica aerogel tiles are listed in Table 4.1.

Table 4.1: Properties of the silica aerogel tiles. The error of the mean value indicates scattering of the value.

Tile	Refractive index	Transmission length (mm)
MEC4-1a	1.0408	41.0
MEC4-1b	1.0411	38.6
MEC4-1c	1.0412	39.2
MEC4-2a	1.0414	40.9
MEC4-2b	1.0414	41.2
MEC4-2c	1.0414	41.7
MEC4-3a	1.0408	41.7
MEC4-3b	1.0410	41.4
MEC4-3c	1.0411	41.7
Mean	1.0411±0.0002	40.8±1.1

These tiles were arranged into three layers. In this prototype detector, the silica aerogel has two functions as a Cherenkov radiator and a shielding matter for range measurement. The thickness of 3 cm was selected so as to stop the β rays from ^{40}K with $K_{\max} = 1.31$ MeV.

On downstream side of the silica aerogel, there are two-layers of B-3 sheets on top and two-layers of Y-11 sheets on the bottom, both with 0.2-mm diameter and the double cladding structure. The effective area of the fiber sheets is 300×100 mm^2. Both ends of the fibers are connected to four PMTs (Hamamatsu R9880U-210) os shown in Fig. 4.1.

4.2 Trigger counter

The trigger counter was placed under the Cherenkov counter. It consists of a sheet made of scintillating fibers (Kuraray SCSF-78MJ) with 0.2-mm diameter with only small energy loss of the β rays emitted from ^{90}Y in the fibers. The β-ray detector used for the environment background measurement (Chap. 3) was adopted as the trigger counter (see Fig. 3.4). The effective area was 300×100 mm^2. The ends of the fibers were connected to PMTs (Hamamatsu R9880U-210).

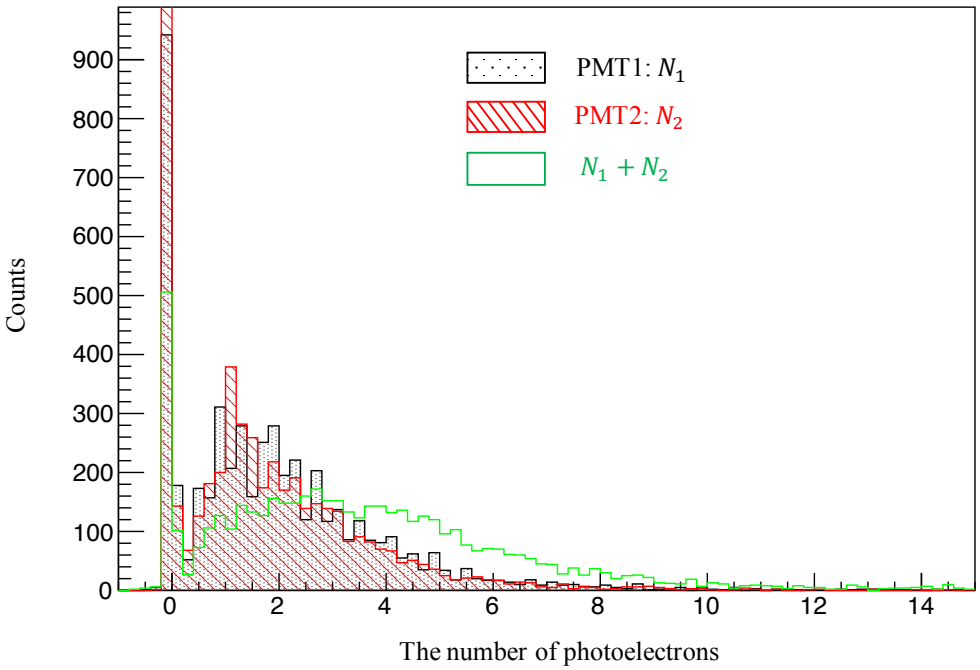

Fig. 4.2: Distribution of the number of photoelectrons observed in the trigger counter with ^{90}Y.

The number of photoelectrons observed in PMT connected to each end of the fibers N_1 and N_2 and the sum of both ends $N_1 + N_2$ are shown in Fig. 4.2, when β rays from ^{90}Y pass through these scintillating fibers. The black, red and green histograms represent N_1, N_1, and $N_1 + N_2$, respectively. Mean numbers are $\langle N_1 \rangle = 1.95 \pm 0.03$ p.e., $\langle N_2 \rangle = 1.73 \pm 0.04$ p.e., and $\langle N_1 + N_2 \rangle = 3.49 \pm 0.04$ p.e.

For suppressing the accidental background originating from PMT thermal noises, the coincidence of two PMTs on the both ends was used as a trigger signal at charged particle incident. The detection efficiency for the β rays was estimated to be $59.5 \pm 0.04\%$ for the threshold of 0.5 p.e. It was calculated as $\langle C_1 \cdot C_2 \rangle$ in binary logic, namely $C_j = 1$ ($N_j > 0.5$) or 0 (otherwise).

4.3 Veto counter

The veto counter is required to cover the trigger and Cherenkov counters. It was produced based on a system using plastic scintillators and wavelength-shifting fibers.

4.3.1 Primary test of the veto counter using cosmic-ray muons

In order to understand the veto counter system using plastic scintillators and wavelength-shifting fiber light guides, a primary test was performed using cosmic-ray muons.

The setup is described below (see Fig. 4.3). Plastic scintillator plates with a size of 100 mm (width) $\times$ 100 mm (long) $\times$ 5 mm (thick) were manufactured by Oyokoken kyogyo Co., Ltd, Japan. Its four side faces were polished but the top and the bottom faces were not polished. The two polished side faces were connected to fiber-sheet light guides using wavelength-shifting fibers, Kuraray Y-11, with a diameter of 0.2 mm. One end of the fiber bundle with a polished surface was connected to a PMT (Hamamatsu R9880U-210). The other end was covered with an aluminized Mylar sheet as a reflection mirror. Two trigger counters with an effective area of 50×50 mm^2 were set above and below the center of the plastic scintillator plate, where the trigger counters consisted of scintillating fibers connected to a PMT (Hamamatsu R9880U-210).

The signals from the trigger counter were input to a coincidence module via a discriminator module whose output signal was a NIM-logical pulse with 10-ns width. The output from the coincidence module was used as a DAQ trigger. The signal from the detector with plastic scintillator and the wavelength-shifting fibers were synchronized with the trigger signal. Thus, an event in the trigger indicated cosmic-ray muon passing through the area overwrapped with the trigger counters.

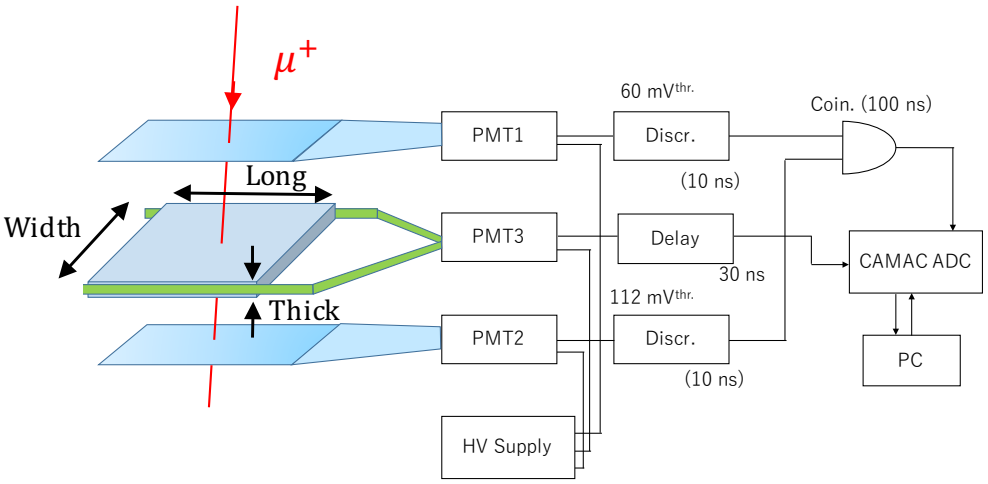

Fig. 4.3: Setup in the primary test of the veto counter.

The mean number of photoelectron was observed to be 4.95 ± 0.05 and the detection efficiency was estimated as $95.8 \pm 1.3\%$ for a threshold of 0.5 p.e. (see Fig. 4.4) for the case in which the Y-11 fibers were 190 mm long and four layers were stacked in the light guide. Single cladding fibers Y-11(300)J were used and the plastic scintillator plate was covered with aluminum foil.

The attenuation length in the plastic scintillator was measured from the relation between the number of photoelectrons via the WLSFs and the width of the scintillator which were 100, 200, 300, and 400 mm. The trigger counters were placed above and below the center of the scintillator plate. The attenuation length was determined to be 312 ± 15 mm by the exponential function fitting of the data. Similarly, the attenuation length of the Y-11 fiber was measured from the relation between the number of photoelectrons and the propagation length along the fibers which were 190, 240, and 520 mm. As a result, the attenuation length was determined to be 523 ± 4 mm.

Different wrapping materials were tested. The materials used were aluminum foil (Al), white paper, white tape made of Teflon, black sheets made of vinyl chloride. In addition, the case of Al attached to the top and the bottom faces as well as white tape attached to the four side faces were tested. The scintillator size was $100 \times 100 \times 5$ mm^3 and the Y-11 length was 190 mm. The result is shown in Fig. 4.5. The largest photoelectron yield was obtained in the case of aluminum foils, i.e., a better light collection was obtained by reflecting photons at the top and the bottom.

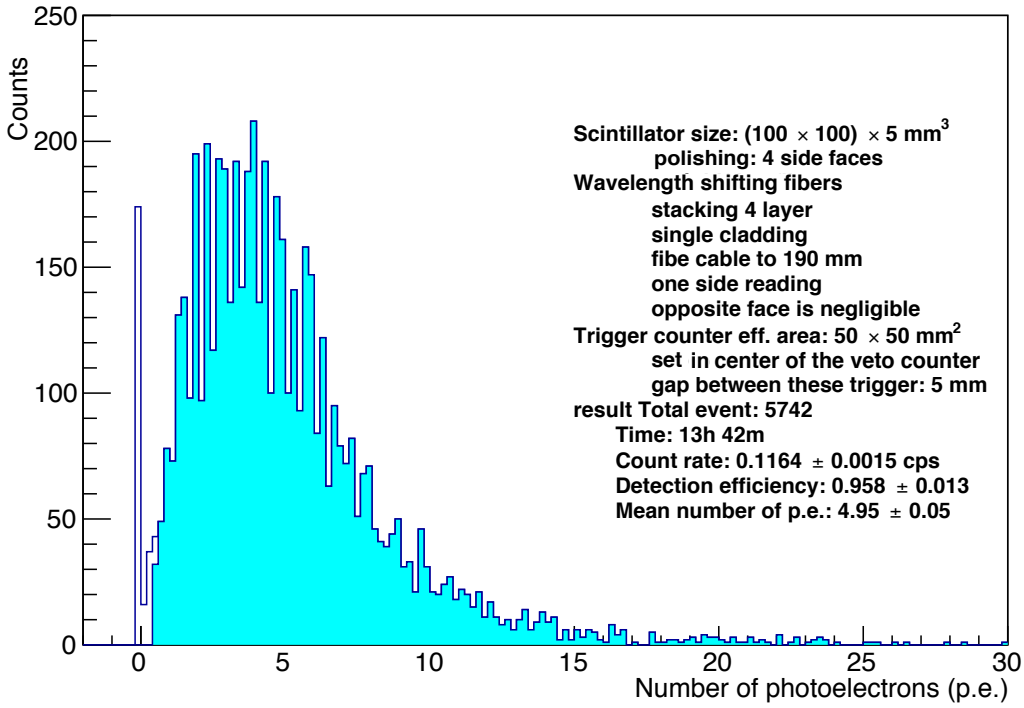

Fig. 4.4: Distribution of photoelectrons observed through the wavelength-shifting fibers when cosmic ray muons passed through the plastic scintillator plate. The cyan filled histogram represents the triggered events over the threshold of 0.5 p.e.

The photon trapping efficiency (10.8%) in the double cladding Y-11(300)MJ fiber was calculated in an optics simulation calculation to be 1.7 times higher than that in the single cladding (6.4%) fiber. The photon yield for the Y-11 fibers with double cladding was measured, where the plastic scintillator size was $100 \times 100 \times 5$ mm^3, and the fiber length was 210 mm, and the scintillator was covered with the aluminum foil. As a result, the mean number of photoelectrons observed was 8.14 ± 0.12 and the detection efficiency was determined to be $98.4 \pm 2.0\%$ for a threshold of 0.5 p.e. The experimental ratio $R_{\rm clad}$ of photon trapping between two type of cladding was given as

$$R_{\rm clad} = \frac{N_2}{N_1} \frac{\exp(-L_1/\lambda)}{\exp(-L_2/\lambda)}, \tag{4.1}$$

where $N_{1,2}$ is the number of photoelectrons in each cladding, $L_{1,2}$ is the fiber

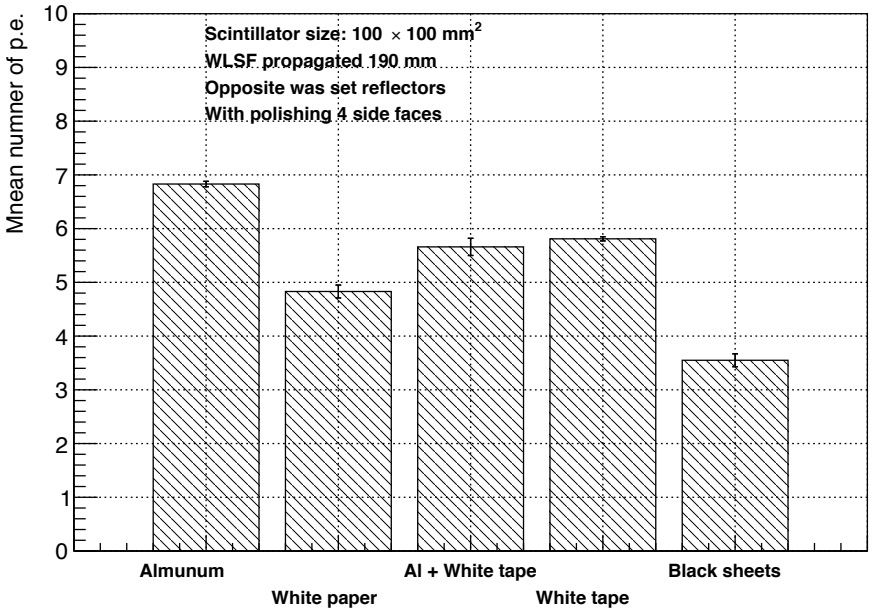

Fig. 4.5: The numbers of photoelectrons in comparison of materials covering the scintillator.

length, and λ is the attenuation length of the Y-11 fiber. The deserved ratio $R_{\rm clad} = 1.71 \pm 0.03$ is consistent with the simulation calculation.

The dependence of the mean number of photoelectrons on the scintillator thickness was measured by stacking the scintillators of 5 mm thickness (up to a maximum of four plates), where the same Y-11 light guide and of length 280 mm and width 20 mm was used the scintillator part was covered with Al foil. In the case of the 20-mm scintillator thickness, the number of photoelectrons increased to 26.9 ± 0.2 and the detection efficiency became $99.7^{+0.3}_{-5.5}\%$. The relation is sufficiently linear with a slope coefficient of (1.30 ± 0.02) mm^{-1} (see Fig. 4.6).

Optical grease (Saint-Gobain BC630) was used to attach the two side scintillators faces to the Y-11 sheets. The grease had a density of 1.06 g/cc, a refractive index of 1.465, and a flat transmission coefficient of approximately 95% in the wavelength range of 280–700 nm. When the grease was put in the gap between these scintillators, the mean number of photoelectrons was 30.1 ± 0.6, and the detection efficiency became $100^{+0}_{-5}\%$, and there was no

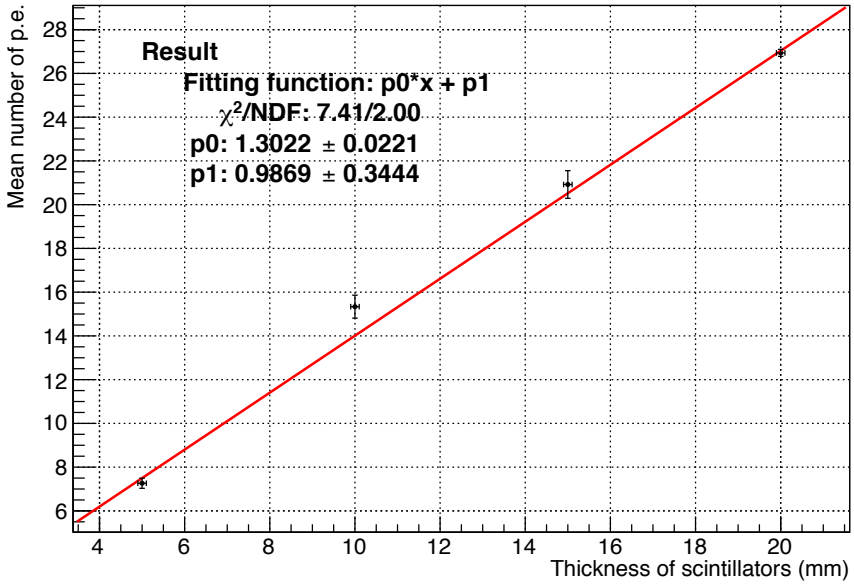

Fig. 4.6: Relation between the numbers of photoelectrons and the scintillator thickness.

event below threshold (see Fig. 4.7 left). In addition, when the grease was also placed in the gap between the scintillators and the Y-11 fibers, the mean number of photoelectrons increased to 36.7 ± 0.3 with a detection efficiency of $100^{+0}_{-2}\%$ (see Fig. 4.7 right).

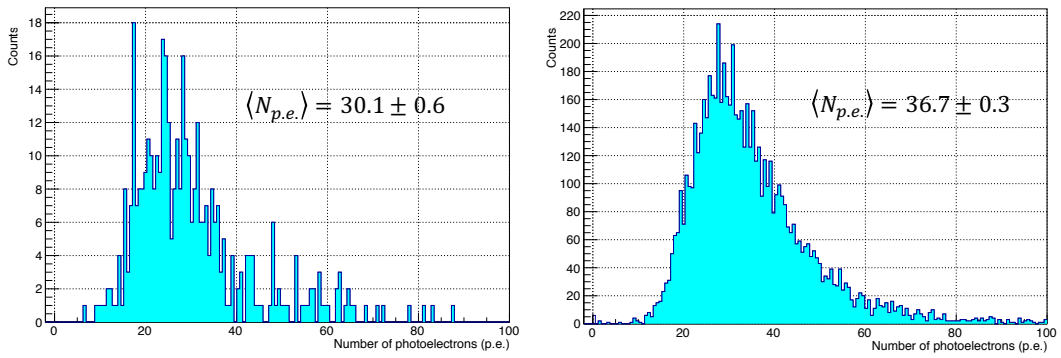

Fig. 4.7: Distribution of the number of photoelectrons when grease was put in the gap between these scintillators (left) and further in the gap between the scintillators and the Y-11 fibers (right).

4.3.2 Components of the veto counter prototype

The veto counter system consists of two units. Each unit has one top side counter, two long side counters, and one short sides counter. The structure of the veto counter system is shown in Fig. 4.8.

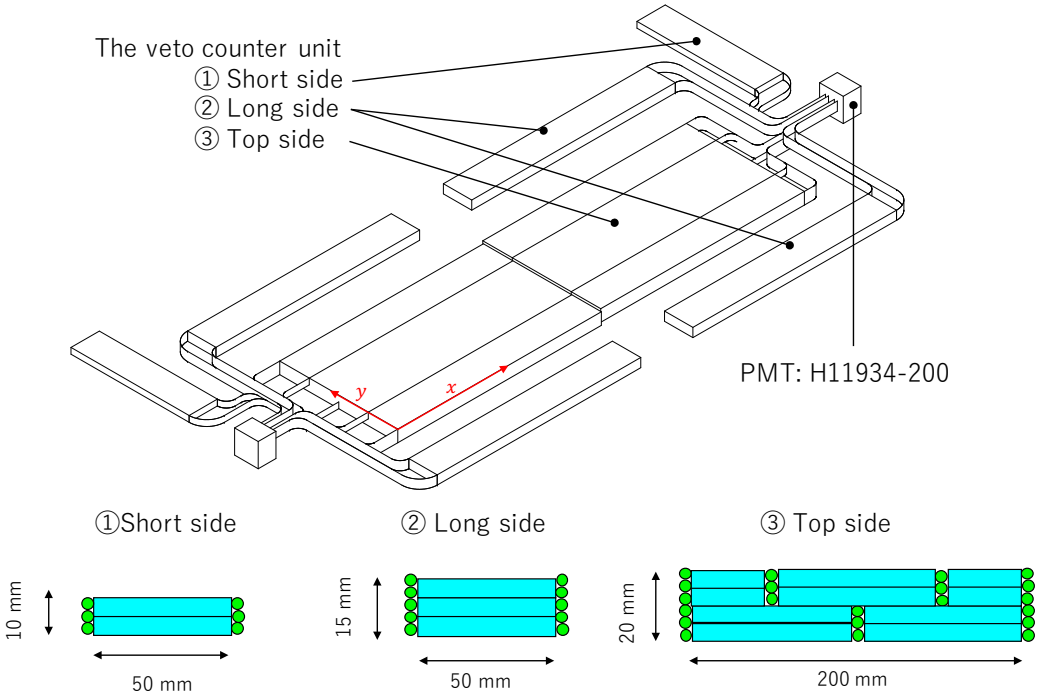

Fig. 4.8: Structure of the veto counter.

The top side counter is a block with a size of $200 \times 350 \times 20$ mm^3 made of four layers of the plastic scintillator with a thickness of 5 mm. Wavelength-shifting fiber (Kuraray Y-11(300)MJ) sheets were connected to both side faces of the block using optical cement (G-Tech EJ-500). The wavelength-shifting fibers were imbedded in a groove on the front face, and two grooves on the back face. The long side counter is a block with a size of $200 \times 50 \times 15$ mm^3 made of three layers of scintillator. The Y-11 fibers were connected to both side faces using optical cement. The short side counter is a block with a size of $200 \times 50 \times 10$ mm^3 made of two layers of scintillator. The Y-11 fibers were also connected to both side faces using optical cement.

One of these fiber ends was connected to a PMT (Hamamatsu H11934-200). The opposite end was connected to a reflector. The light propagation

length in the fibers was approximately 300 mm. The veto counter had an inner volume of $170 \times 680 \times 50$ mm^3.

4.3.3 Performance

The uniformity of photon yields was measured by using cosmic-ray muons passing through the veto counter. The distribution of the photoelectron number $N_{p.e.}$ is shown in Fig. 4.9 (left). A mean number $\langle N_{p.e.} \rangle = 55.0 \pm 0.8$ was observed when the muons passed through the center of the unit. The right figure shows the relation between $\langle N_{p.e.} \rangle$ and the muon-hit position x along the Y-11 fibers. The open black circles, red squares, and green triangles are, respectively, the data for $y = 150 \pm 25$ mm, 100 ± 25 mm, and 50 ± 25 mm. As a result, the mean number of photoelectrons was observed to be 50-60 at any position; thus, this veto counter has sufficient performance for the suppression of cosmic-ray-muon events.

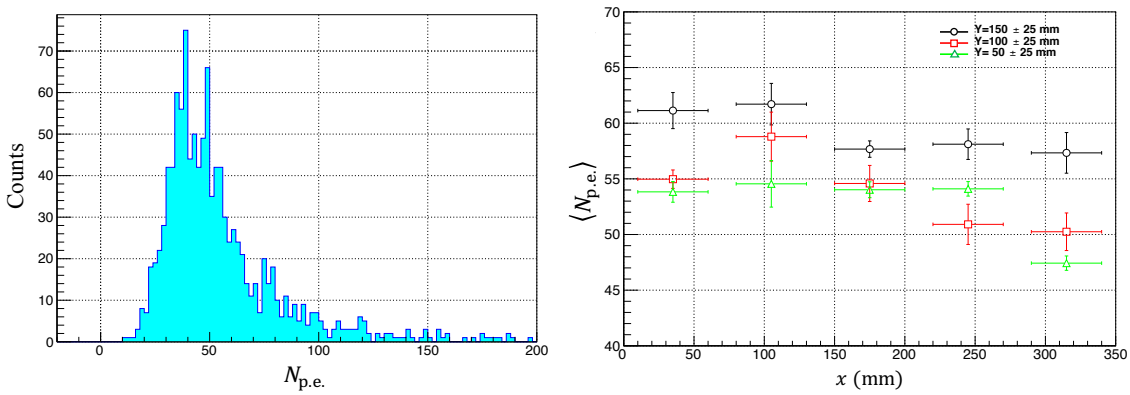

Fig. 4.9: Number of photoelectrons $N_{p.e.}$ in the veto counter (left) and the relation between the mean $N_{p.e.}$ and the muon-hit position (right).

4.4 Electronics

The PMTs were supplied with 1200 V by high voltage supply units (REPIC RP-1637BS). All PMT signals in this detector were fed to discriminators (REPIC RP-1637AS). The coincidence signals of the trigger counter and the Cherenkov counter without a hit in the veto counter were counted under the condition of $\prod_{j=1}^{2} C_j^{\mathrm{Trig}} = 1$ for the trigger, $\sum_{j=1}^{4} C_j^{\mathrm{AC}} \geq 2$ for the Cherenkov counter, and $\sum_{j=1}^{2} C_j^{\mathrm{Veto}} \geq 1$ for the veto counter. Here, $C_j = 1$ ($N_j > 0.5$) or 0 (other).

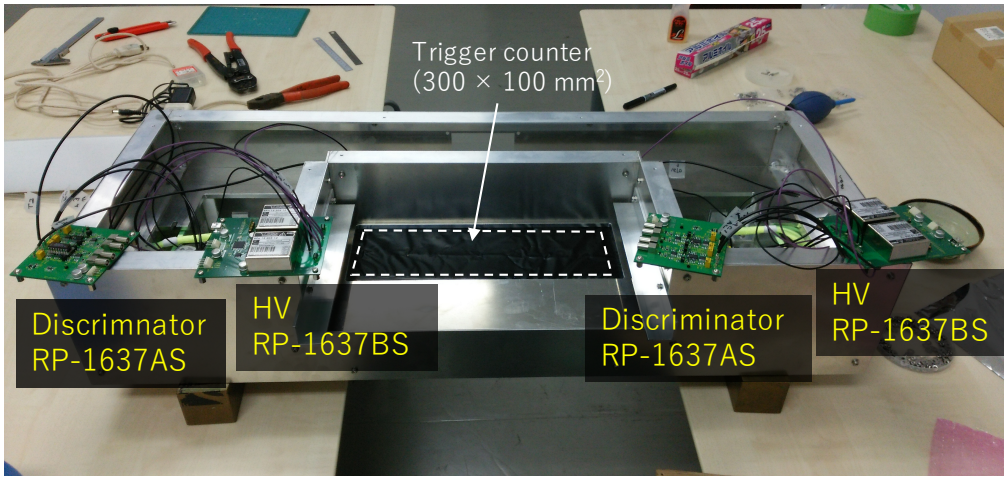

Fig. 4.10: Picture of the prototype detector and electronics hardwares.

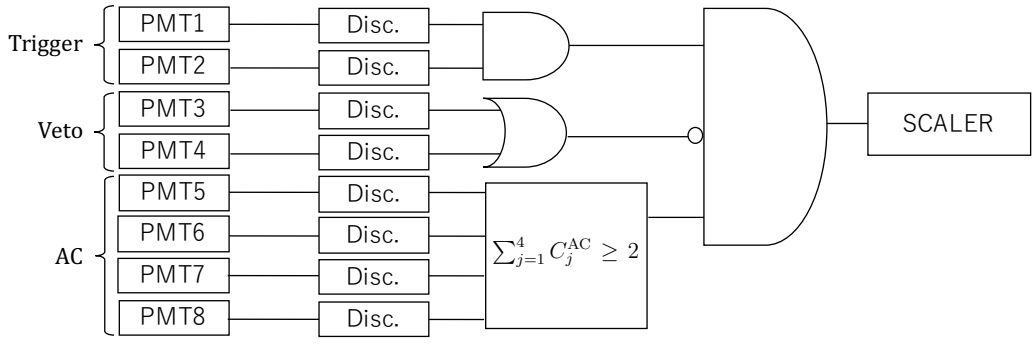

Fig. 4.11: The signal logics.

4.5 Shielding by lead and brass blocks

This detector was shielded externally by lead and brass blocks for the suppression of γ rays emitted from ^{214}Bi and ^{208}Tl in the surrounding concrete blocks (see Fig. 4.12). Lead plates with 32-mm thickness were placed under the detector. On the short sides, lead blocks with 50-mm thickness were placed. On the long sides, lead plates with 32-mm thickness were placed on the the brass blocks of 50-mm thickness. On the top of the detector, lead plates with 32-mm thickness were put on the the brass blocks with 25-mm thickness. The densities of lead and brass are 11.35 and 8 g/cm^3, respectively. The total attenuation coefficient for 2-MeV γ rays in lead is 4.5×10^{-2} g/cm^2. Thus, 3.2-cm thick lead, 5-cm thick lead, and 5-cm thick brass suppressed 2-MeV γ rays with the fraction of 83.5%, 92.4%, and 83.7%, respectively. For 99% suppression of the γ rays, 9-cm thick lead and 13-cm thick brass would be required.

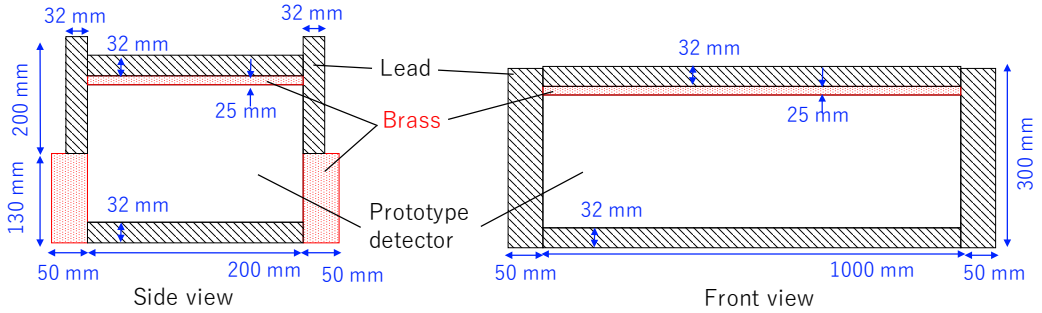

Fig. 4.12: A schematic cross section with side view (left) and front view (right) for shielding by lead and brass blocks.

Chapter 5

Performance of the prototype detector

The performance of the prototype detector was estimated using radioactive sources of ^{90}Sr, ^{137}Cs, and ^{40}K is presented in this Chapter. They were placed one by one under the center of the detector, and the one hour counting rate was measured dozens of times. The purpose of the detector was to identify a sample that may contain ^{90}Sr. In a performance test of the prototype detector, the sensitivity, namely the limit of ^{90}Sr concentration, was determined for different threshold conditions. The tail of counting rate histogram, which is lower than the threshold was regarded as the in-efficiency of ^{90}Sr detection. Then, the "signal model" to describe the detection efficiency was developed based on the experimental data.

5.1 Radioactivity of sources

Radioactive sources of ^{90}Sr, ^{137}Cs (delivered by Japan Radioisotope Association (JRA)), and ^{40}K (described below) were used in this test. The radioactivities of ^{90}Sr and ^{137}Cs were calculated to be 23.6 ± 0.3 kBq and 26.0 ± 0.5 kBq, respectively, from the initial calibration of 37 kBq at JRA for both.

Because ^{40}K sources are not available commercially, potassium chloride (KCl) was used as the ^{40}K source. The KCl sample had a mass of 30.0 ± 0.1 g and a radioactivity of 498 ± 2 Bq from ^{40}K. It was obtained from Hayashi Pure Chemical Ind., Ltd. with a purity $\gtrsim 99.5\%$.

5.2 Counting rate

The one hour counting rate measurement was repeated dozens of times and a histogram of THE one-hour count was produced. The background rate without a sources, and the counting rates for the source of ^{90}Sr, ^{137}Cs and ^{40}K are shown in Fig. 5.1, as the black, blue, red, and green histogram, respectively. The sources were placed under the center of the detector for the one-hour measurement. The background rate without sources was $N_{BG} = (35.2 \pm 6.0)$ h^{-1} by a Gaussian fitting of the peak with $\chi^2/\mathrm{NDF} = 4.73/11$, where NDF is the number of degrees of freedom. Typically, this background distribution is regarded as a Poisson distribution, $P(n, \nu) = e^{-\nu}\nu^n/n!$, where n is the counting rate and ν is the mean counting rate. Since n is large, the distribution $P(n, \nu)$ is approximated by a Gaussian distribution. Because the statistical variation can be changed by fluctuation effects of the detector, the distribution was analysed considering the deviation from the Poisson function. The deviation factor α was introduced as the ratio of the standard deviation σ to the square root of the mean ν ($\alpha = \sigma/\sqrt{\nu}$), thus giving $\alpha_{\mathrm{BG}} = 1.01 \pm 0.02$.

The counting rate for ^{90}Sr was $N_{\mathrm{Sr}} = (1.45 \pm 0.01) \times 10^5$ h^{-1} by a Gaussian fitting with $\chi^2/\mathrm{NDF} = 12.1/18$ and $\alpha_{\mathrm{Sr}} = 2.80 \pm 0.22$, where the contribution from the background was negligible.

The counting rates for ^{137}Cs and ^{40}K were $N_{\mathrm{Cs}} = (159 \pm 8)$ h^{-1} and $N_{\mathrm{K}} = (45.1 \pm 6.9)$ h^{-1}, respectively. The contribution from the background is not negligible in the calculation of α for these sources; therefore, it was necessary to subtract the background contribution.

5.3 Signal model

The "signal model" was developed based on the experimental data. The background peak form is consistent with a Poisson distribution as indicated by the small χ^2/NDF. The background was treated as a Gaussian distribution $\mathit{\Gamma}_{\mathrm{BG}}(n)$ to simplify the model

$$\mathit{\Gamma}_{\mathrm{BG}}(n) = \frac{1}{\sqrt{2\pi\sigma_{\mathrm{BG}}^2}} \exp\left\{-\frac{(n-\nu_{\mathrm{BG}})^2}{2\sigma_{\mathrm{BG}}^2}\right\}, \tag{5.1}$$

where n is the counting rate, $\nu_{\mathrm{BG}} = 35.1$ h^{-1}, and $\sigma_{\mathrm{BG}} = 6.0$ h^{-1}. The counting rate distribution for the source x can be represented as a convolute

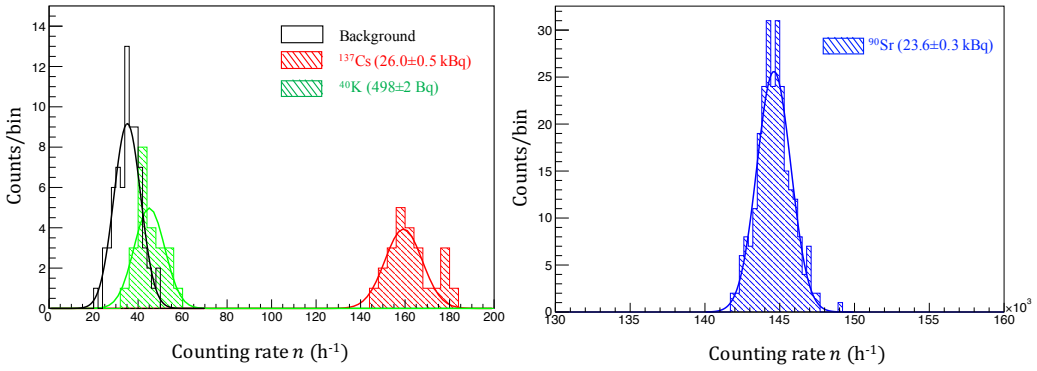

Fig. 5.1: The background rates and count rate of ^{137}Cs and ^{40}K (left) and ^{90}Sr (right).

integration with the background rate

$$\Gamma_x(n) = \int d\tilde{n}\ \phi_x(\tilde{n}) \cdot \Gamma_{\rm BG}(\tilde{n} - n), \tag{5.2}$$

where $x = {}^{90}$Sr, ^{137}Cs, and ^{40}K.

I developed the signal model for the reconstruction of the distribution $\phi_x(n)$, which is given as

$$\phi_x(n) = \frac{e^{-\nu/\alpha^2}(\nu/\alpha^2)^{n/\alpha^2}}{\Gamma(n/\alpha^2 + 1)}, \tag{5.3}$$

where ν is the mean counting rate, α is the deviation factor which was obtained by fitting data, and $\Gamma(n)$ is the Gamma function. This model performs the transformation $\nu \to \nu/\alpha^2$ and $n \to n/\alpha^2$ in the Poisson function $P(n, \nu)$.

The χ^2 dependence on the free parameter α is shown in Fig. 5.2, where $\chi^2 = \sum_i \{y_i - \phi(n_i, \alpha)\}^2/\sigma_i^2$. The black dots are the $\chi^2(\alpha)$ and the red line is a quadratic fitting function which can interpolate the dots. The best fit αs were determined to be $\alpha_{Cs} = 0.532 \pm 0.044$ with $\nu_{Cs} = 124.1 \pm 0.2$ and $\alpha_K = 1.067 \pm 0.106$ with $\nu_K = 9.7 \pm 0.2$ as the minimum of this quadratic curve (listed in Table 5.1).

As the results of the fitting, the distribution functions $\phi_x(n)$, $\Gamma_x(n)$, and $\Gamma_{\rm BG}(n)$ were determined. These are as plotted in Fig. 5.3 together with the data. The filled red and blue areas are, respectively, the deduced signal functions $\phi_{\rm Cs}(n)$ and $\phi_{\rm K}(n)$. The doted black area and the red line are the

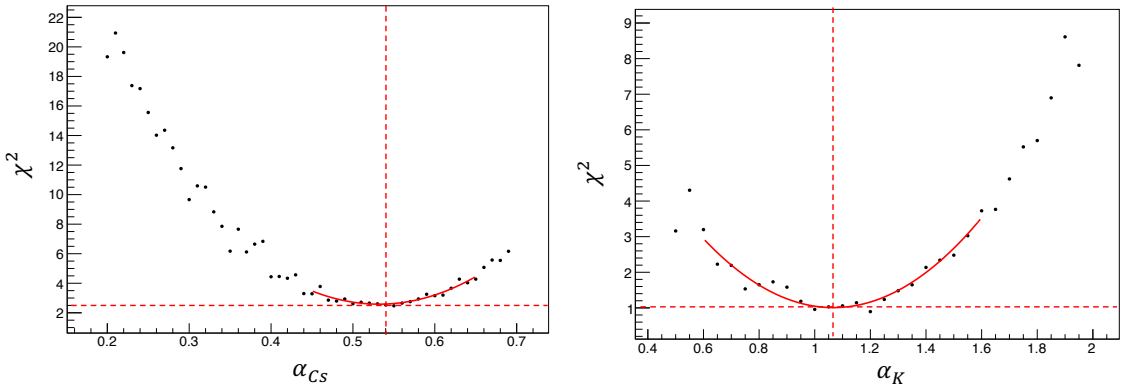

Fig. 5.2: Fitting χ^2 depending on the free parameter α for ^{137}Cs (left) and ^{40}K (right).

background rate of the data and the simulated $\Gamma_{\mathrm{BG}}(n)$, respectively. The hatched red area and magenta line are the counting rate distribution for ^{137}Cs and simulated $\Gamma_{\mathrm{Cs}}(n)$, respectively. The hatched green area and the blue line are the counting rate distribution for ^{40}K and simulated $\Gamma_{\mathrm{K}}(n)$, respectively.

It is considered that the mean counting rate ν is proportional to the radioactivity intensity of the source A, i.e., $\nu = kA$. The coefficient for ^{137}Cs and ^{40}K are $k_{Cs} = (4.77 \pm 0.09) \times 10^{-3}$ Bq^{-1} h^{-1} and $k_K = (1.95 \pm 0.04) \times 10^{-2}$ Bq^{-1} h^{-1}, respectively.

For ^{90}Sr α_{Sr} and k_{Sr} were measured with increasing the intensity of the radioactivity as shown in Fig. 5.4 left and right, respectively. The black dots are the data. k_{Sr} tends to decrease with the increase of the mean counting rate ν. It is considered that there is a source position dependence of the sensitivity in the detector because the added sources were away from the detector center as the intensity of radioactivity is increased. A dependence of α_{Sr} on ν was not observed. Therefore, the average of values of $\alpha_{Sr} = 2.50 \pm 0.50$ and $k_{Sr} = 6.23 \pm 0.13$ Bq^{-1} h^{-1} were obtained. In Fig 5.4, the red line is the mean value and hatched red area represents the standard deviation. Therefore, in the measurement of the ^{90}Sr concentration, the prototype detector can suppress the accidental background from ^{137}Cs and ^{40}K by factors of $k_{Cs}/k_{Sr} = (7.65 \pm 0.21) \times 10^{-4}$ and $k_K/k_{Sr} = (3.13 \pm 0.09) \times 10^{-3}$, respectively.

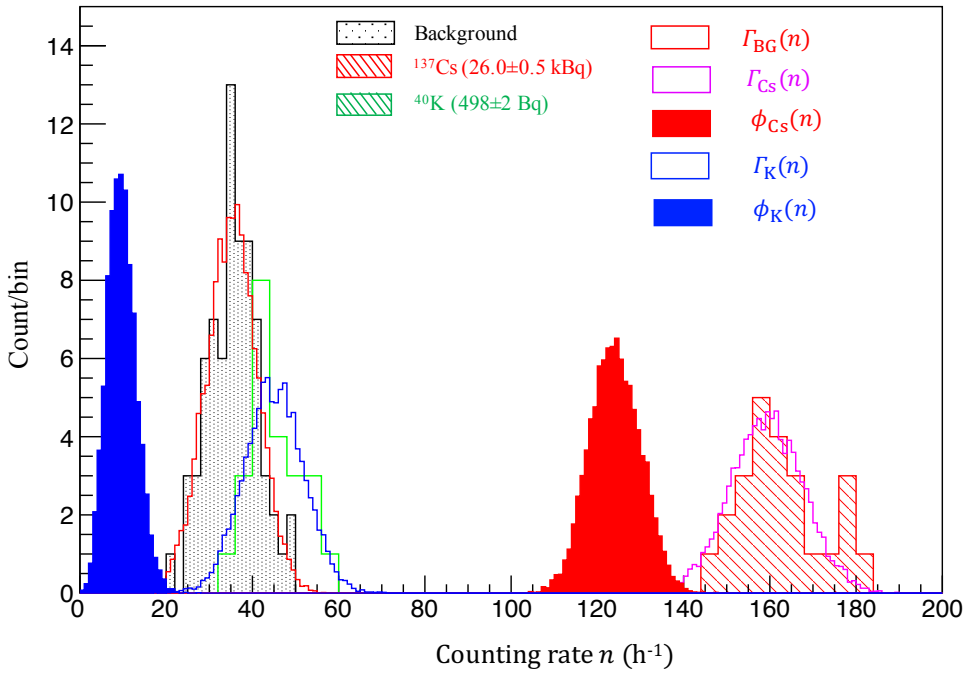

Fig. 5.3: Distribution of counting rates in the signal model for ^{137}Cs and ^{40}K, and the comparison with the data.

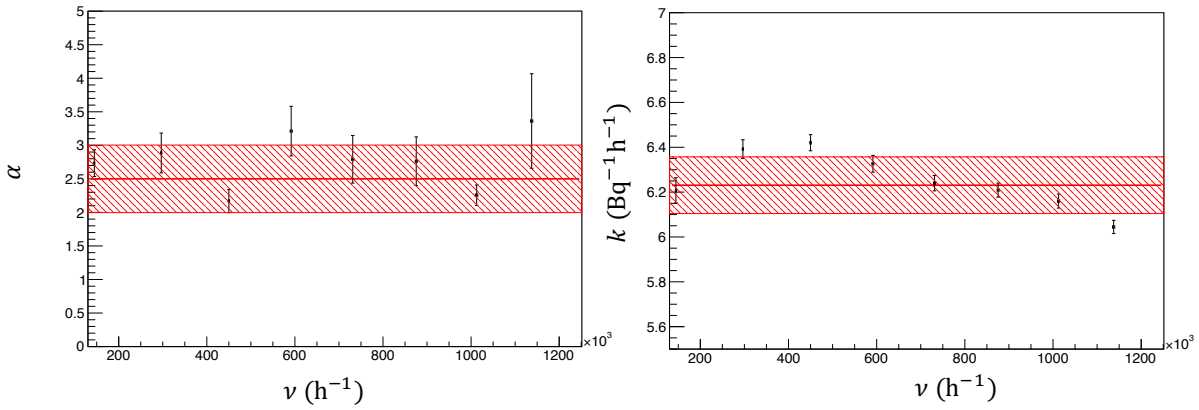

Fig. 5.4: α and k depending on ν for the ^{90}Sr.

Table 5.1: Best fit parameter in the signal model

Source	α	k ($\mathrm{Bq^{-1}\ h^{-1}}$)
^{90}Sr	2.50 ± 0.50	6.23 ± 0.13
^{137}Cs	0.532 ± 0.044	$(4.77 \pm 0.09) \times 10^{-3}$
^{40}K	1.067 ± 0.106	$(1.95 \pm 0.04) \times 10^{-2}$

5.4 Correction of the position dependence

The effective area of the detector is 300×100 mm^2. The detector has a response depending on the source position. Because β rays from the ^{90}Sr source are emitted isotopically, it is clear that the yield is less at the edge than at the center. The relation of the source position and k_{Sr} is shown in Fig. 5.5. The left panel shows the two-dimensional color-histogram for position X and Y. The right figure shows k_{Sr} as a function of X. The black, red, green, blue, and yellow bars are for Y = 10, 30, 50, 70, and 90 mm, respectively. The coefficient was corrected to be $\tilde{k_{\mathrm{Sr}}} = (4.11 \pm 1.91)$ $\mathrm{Bq^{-1}\ h^{-1}}$ taking an average of these values.

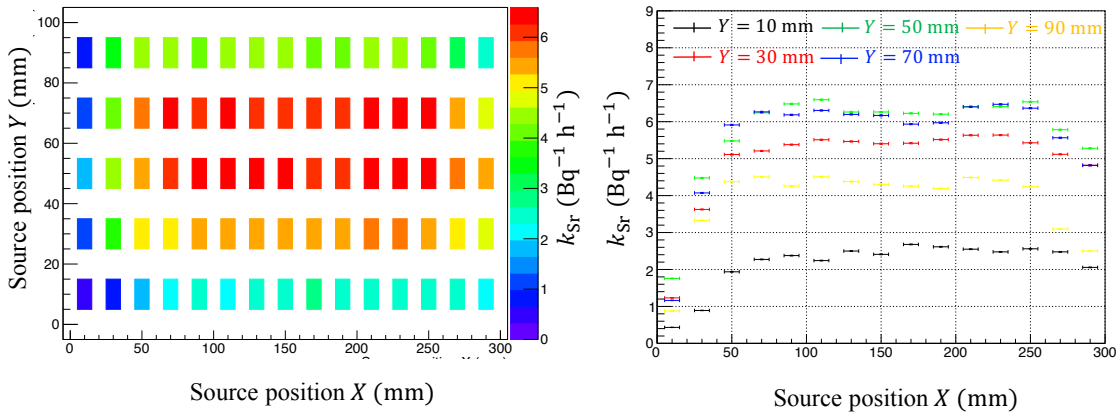

Fig. 5.5: Source position dependence of k_{Sr}.

5.5 Detection efficiency and limit

The detection efficiency of the prototype was estimated using the signal model. It is assumed that the count rate threshold was set at 3σ from the mean of the background rate. The background and the corrected signal of 10-Bq ^{90}Sr are shown in Fig. 5.6. The blue line is the background, the red hatched area is the histogram of the ^{90}Sr count rate (the mean at 74.9 h^{-1}), and the red double-hatched area represents the events with count rate above the threshold. These histograms are normalized to have an integral of 1. The ratio of the events above the threshold in total signal was defined as the detection efficiency of ^{90}Sr, which is therefore $\eta_{3\sigma}(10\ \mathrm{Bq}) = 91.6 \pm 0.3\%$ for 10-Bq ^{90}Sr.

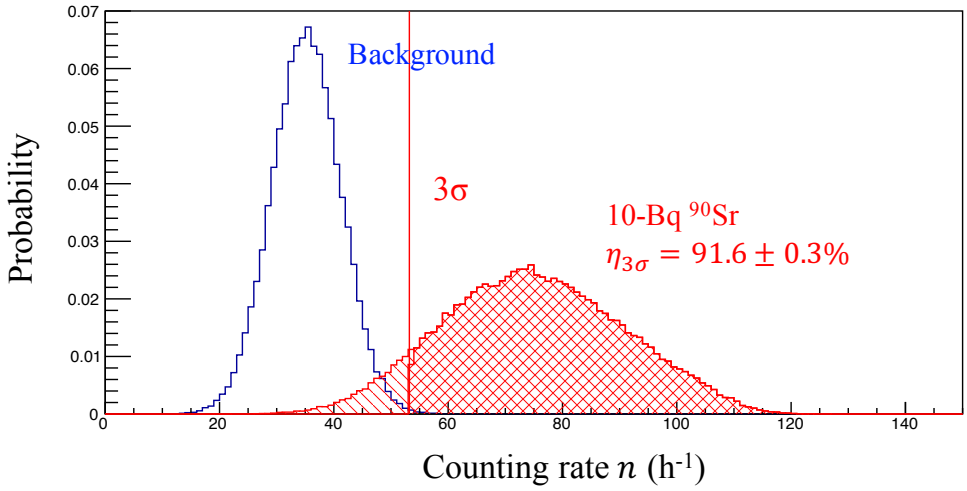

Fig. 5.6: Distribution of the background and 10-Bq ^{90}Sr counting rate at one hour measurement.

The detection efficiency dependence on the ^{90}Sr radioactivity for a one-hour measurement is shown in Fig. 5.7. The black, red, and green dots represent, respectively, the efficiency curves for the threshold conditions of 1σ, 2σ, and 3σ. The least ^{90}Sr radioactivity A' satisfying the efficiency of more than 50% was determined to be $A'^{50\%}_{1\sigma} = 1.4$ Bq, $A'^{50\%}_{2\sigma} = 3.0$ Bq, and $A'^{50\%}_{3\sigma} = 4.6$ Bq. Similarly, the least ^{90}Sr radioactivity satisfying the efficiency over more 90% was determined to be $A'^{90\%}_{1\sigma} = 5.4$ Bq, $A'^{90\%}_{2\sigma} = 7.6$ Bq, and $A'^{90\%}_{3\sigma} = 9.6$ Bq. The least radioactivity indicates the observable lower limit

in the sample for a one-hour measurement. The efficiency for ^{137}Cs and ^{40}K was determined in the same way as for ^{90}Sr. The least radioactivity satisfying 50% and 90% efficiency for 1, 2, and 3 σ thresholds were thus determined (Table 5.2).

The detection limit has often been defined as the minimum radioactivity satisfying the relation of $\langle \Gamma_{\mathrm{Sr}}(n) \rangle > \langle \Gamma_{\mathrm{BG}}(n) \rangle + 3\sigma$, where σ is the standard deviation of $\Gamma_{\mathrm{BG}}(n)$. Therefore, the detection limit corresponds to the lower limit of 50% efficiency in the 3-σ threshold condition ($A'^{50\%}_{3\sigma}$).

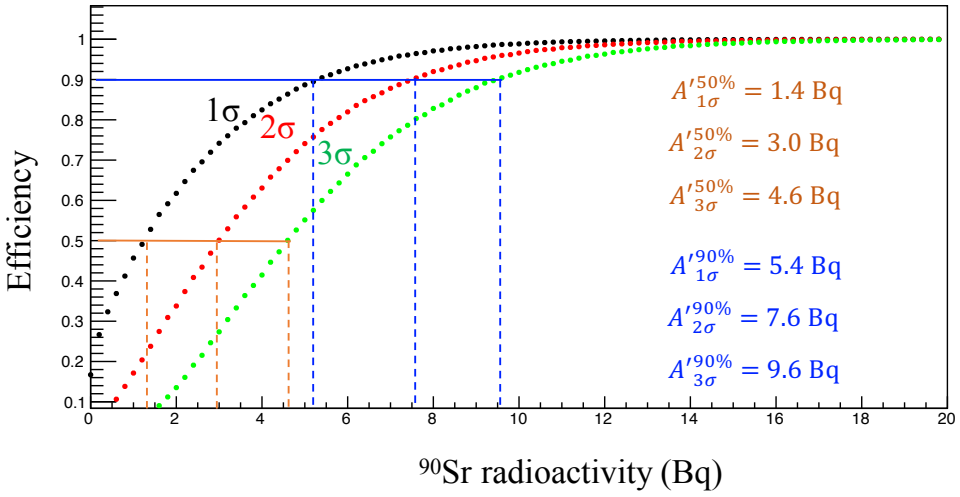

Fig. 5.7: Detection efficiency as a function of the ^{90}Sr radioactivity related to the threshold condition for a one-hour measurement.

5.6 Concentration

In the current detector, the effective area is $S = 30 \times 10$ cm^2, and thus the detection lower limit of concentration was $A'^{50\%}_{3\sigma}/S = 0.0153$ Bq/cm^2. In the β-rays contamination inspection, the ^{90}Sr concentration in a sample should be measured after the sample was dried and made into a thin paste because otherwise the β rays deposit energy in the sample.

Here, it is assumed that the density of the sample is 1 g/cm^3. Because approximately 70% of the seafood sample volume is water, it is considered that the sample volume is compressed to 30% by drying, namely the compression

Table 5.2: Least radioactivity A' for 50% and 90% efficiency in a one-hour measurement when the threshold is set at 1σ, 2σ, and 3σ.

Source	Efficiency	Least Radioactivity A' (Bq)		
		1σ	2σ	3σ
^{90}Sr	50%	1.4	3.0	4.6
	90%	5.4	7.6	9.6
^{137}Cs	50%	1.3 $\times 10^3$	2.5 $\times 10^3$	3.8 $\times 10^3$
	90%	3.1 $\times 10^3$	4.5 $\times 10^3$	5.8 $\times 10^3$
^{40}K	50%	0.32 $\times 10^3$	0.65 $\times 10^3$	0.94 $\times 10^3$
	90%	0.80 $\times 10^3$	1.12 $\times 10^3$	1.44 $\times 10^3$

factor is $\varepsilon = 0.3$. When the dried sample thickness is 1 mm, the upper limit of the weight which can be measured by the prototype detector is $m = 30$ g (corresponding to the original of $m/\varepsilon = 100$ g). Therefore, the lower limit to detect ^{90}Sr concentration in a one-hour measurement was estimated to be $A'^{50\%}_{3\sigma}\varepsilon/m = 46$ Bq/kg. This limit is lower than the food contamination permissible limit of 100 Bq/kg defined by Ministry of Health, Labour and Welfare, Japan, in 2012 [25].

Furthermore, in the case of seawater, the lower limit of dried seawater in a one-hour measurement is estimated to be $A'^{50\%}_{3\sigma}\varepsilon/m = 1.5$ Bq/L with the original volume of $m/\varepsilon = 3$ L, because it is of most made of water (99% or more) with the compression factor $\varepsilon = 0.01$ by drying. On the other hand, the samples have potassium in nature. For example, seawater has 0.39 g/L of K^+ ions on average, thus giving ^{40}K activity of 12.1 Bq/L, since the specific radioactivity of ^{40}K is 2.6×10^6 Bq/g and the ^{40}K isotopic abundance is 0.117%. Because the detection efficiency is $\eta_{3\sigma}(36.3\ \text{Bq}) = 0.23\%$ for the 3 L seawater, the influence of ^{40}K is negligibly small for the ^{90}Sr measurement.

5.7 Results

The detector performance was given in terms of the detection efficiency curve (see Fig. 5.6) using the signal model developed based on data. Because the ratio of $k_{\text{Cs}}/k_{\text{Sr}}$ and $k_{\text{K}}/k_{\text{Sr}}$ are 10^{-4} – 10^{-3}, the detector can observe β rays from ^{90}Y effectively even in the presence of the backgrounds of ^{137}Cs and ^{40}K. For the inspection of the radioactivity contamination of a sample, the detection limit of ^{90}Sr can be reduced by decreasing the threshold, however

the probability of misidentification will increase.

Chapter 6

Summay

The basic properties of a Cherenkov detection system for ^{90}Sr using silica aerogel and wavelength-shifting fibers have been studied by several test experiments and simulation calculations. The optical collection efficiency for the fibers to absorb Cherenkov photons from the side face and to propagate to both ends was estimated to be 1.0–1.4%. The Cherenkov photons from the aerogel by ^{90}Y were observed to be 2.4 ± 1.3 s^{-1} using a 23.6 kBq ^{90}Sr source. This result was consistent with the simulated value of 2.35 s^{-1} using (1) the models of ^{90}Sr and ^{90}Y β-rays energy spectra, (2) the optical spectra of emitted Cherenkov photons, and (3) the wavelength-shifting absorption and emission spectra. It was found in the prototype test that the system using wavelength-shifting fibers can suppress the accidental noise down to $11.0 \pm 1.1\%$ due to the extended effective detector area in comparison with the conventional method of direct-PMT readout.

The environmental radiation which affects the detector performance was investigated. The γ rays from ^{214}Bi, ^{208}Tl, and ^{40}K in the building concrete wall or floor were observed in the energy spectroscopy using a BGO crystal. The Cherenkov detector should suppress the γ rays from these radioisotopes in the ^{90}Sr contamination inspection of the samples. In a test measurement on the roof, it was found that the ^{214}Bi concentration was less than 100 Bq/m^3 in air. For inspection of ^{90}Sr in the detector with air volume of 5-10 L, the concentration of approximately 0.5–1 Bq is negligible. The β rays originating from the radon progenies in the air was measured using polyethylene sample sheets which were exposed in the windless room air. The surface concentration was saturated to 18 Bq/m^2 with the time that the samples were exposed in the room air. It was found that this effect is not

negligible, thus the sample should be exposed to the air. The adsorption ratio among ^{218}Po, ^{214}Pb, and ^{214}Bi on the sample sheets were estimated from the decay curve of the counting rate. This result suggests that we can reject the scenario that only ^{218}Po falls just after the radon decay in the air. Namely, the potential of internal exposures by inhalation of the radon progenies in the air is indicated. This suggestion would be a clue to clear the occurring mechanism of the lung cancer among the non-smokers in the future.

The prototype detector was produced and its performance was estimated using radioactive sources. Cosmic-ray veto counters were placed on top and four sides of the Cherenkov detector, and they had an efficiency of more than 99.9% for cosmic-ray muons. Furthermore, the detector was shielded externally using lead and brass blocks for the suppression of environmental radiation. In the performance estimation, the one-hour counting rates were measured using ^{90}Sr, ^{137}Cs, and ^{40}K sources a dozen times. A "signal model" which reproduces these counting rate histograms was developed. The source position dependence of the sensitivity was corrected. The detection limit of ^{90}Sr in a one-hour measurement was determined to be 4.6 Bq using this model, where the detection limit was defined as the lower limit of 50% efficiency in a 3-σ threshold condition ($A'^{50\%}_{3\sigma}$). The detectable concentration lower limit was calculated to be 46 Bq/kg for dried seafood samples, thus it was demonstrated that the current prototype detector can be applied to the inspection of ^{90}Sr contamination. In the future, a large-size detector would be produced with an improvement to reduce the lower limit by enlarging the detector effective area, since the concentration lower limit is inversely proportional to the effective area.

Appendix A

PMT Calibration

In this study, Hamamatsu PMTs, (1) R1250-03, (2) R9880U-210, and (3) H11934-200, were used. In this appendix, the gain calibration, the noise estimation are described.

A.1 Setup

Fig. A.1 (top) shows the setup of the PMT calibration test. The high voltage of 1.2–1.4 kV was supplied to the PMT (R9880U-210). The analog signal from the PMT anode was input to CAMAC ADC. The LED with 365 nm was used as a light source in the test. A function generator (Agilent 33250A) gave a pulse current to the LED for emission photons with 1 kHz. Another output of the function generator (TTL-Type logic signal) with the same timing as the current pulse was converted to a MIN logic pulse using a TTL-NIM converter module. This logical signal was adjusted to 200-ns width with a gate generator module and fed to the ADC Gate as a trigger signal.

In the oscilloscope view shown in Fig. A.1 (bottom right), the magenta and yellow lines are the trigger and PMT analog signal, respectively. This signal corresponds to 1 p.e. and has pulse height of approximately 50 mV.

A.2 Gain

The ADC distribution is shown in Fig. A.2 (left). The red lines are Gaussian fitting functions for the pedestal and for the 1 p.e. peak. The

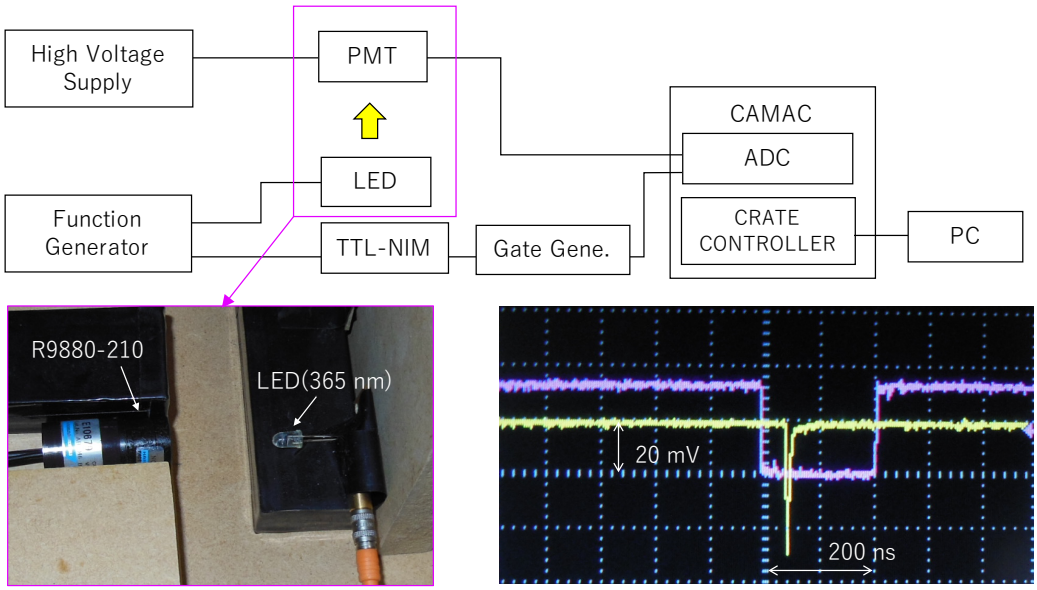

Fig. A.1: Setup of calibration test for PMTs. Schematic for diagram (top), picture of the setup (bottom left), and output signals checked by the oscilloscope (bottom right).

discrete signals were observed by photoelectron effect in the single photon region. The gap between the pedestal and the 1 p.e. peak corresponds to the gain $\mu(V)$ given as

$$\mu(V) = \frac{(M_1 - M_0)k_C}{|e|}, \tag{A.1}$$

where M_0 and M_1 are the ADC values for pedestal and 1 p.e. peak, respectively, k_C is the CAMAC ADC conversion coefficient (~ 0.26 pC/ADC), and e is the elementary charge. This gain depends on supplied voltage as

$$\mu(V) = \alpha V^{\beta}. \tag{A.2}$$

In Fig. A.2 (right top), the black dots are data and the red line is the fitting function of Eq. (A.2), where $\alpha = (1.3 \pm 1.0) \times 10^{-5}$, $\beta = 3.9 \pm 0.1$ with $\chi^2/\mathrm{NDF} = 3.03/9$. The measurement accuracy was $\sigma_\mu/\mu < 8\%$, which was determined as a deviation with the data and fitting function.

A.3 Noise ratio

According to the measured gain, the photoelectrons distribution is shown in Fig. A.3 (left), which is a dark count. The noise ratio was defined as 0.5-p.e. efficiency of dark count. The supplied voltage dependence for the noise ratio is shown in Fig. A.2 (right), and the noise ratio was less than 10^{-4}.

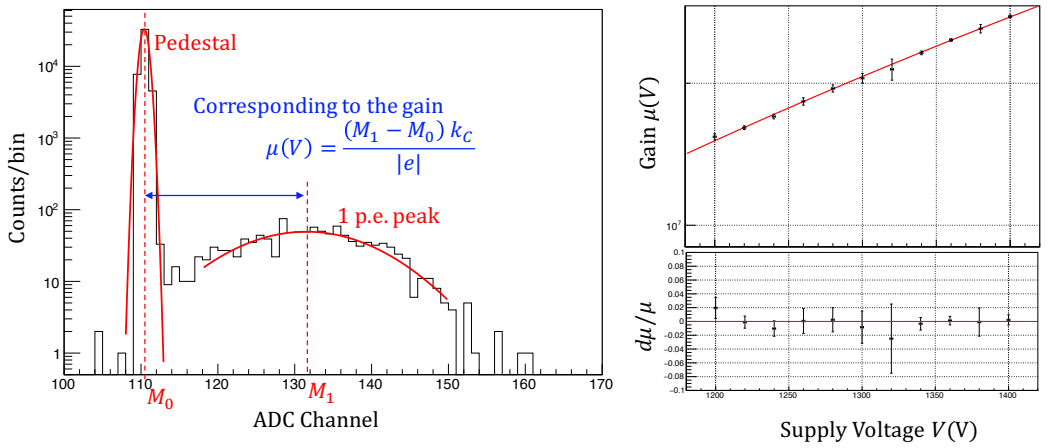

Fig. A.2: ADC distribution (left), Gain depending on supplied voltage (right top) and measurement accuracy (right bottom).

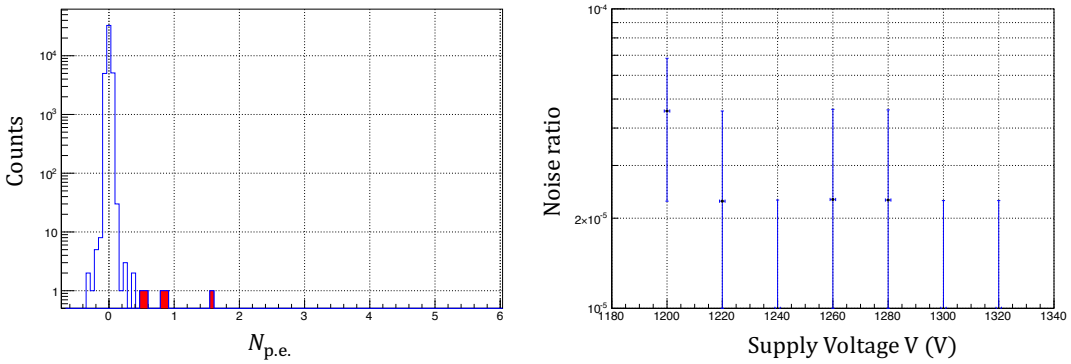

Fig. A.3: Converted distribution (left) and relation between the noise ratio and supplied voltage.

Appendix B

Energy calibration and resolution of the BGO detector

The energy calibration of the BGO detector was performed using ^{137}Cs, ^{137}Na, and ^{60}Co sources. The energy spectra of these radioisotopes are shown in Fig. B.1. The blue, black, magenta, and green histograms represent ^{137}Cs, ^{22}Na, ^{60}Co, respectively, and the background without source is also shown as "no source". Peaks are seen at 511 keV and 1,274 keV for ^{22}Na, 662 keV for ^{137}Cs, and 1,173 keV and 1,332 keV for ^{60}Co. Sum energy peaks are 1,785 keV for ^{22}Na and 2,505 keV for ^{60}Co. The relation between the ADC value and the energy is confirmed to be linear as ADC$= kE_\gamma +$ Const with the conversion coefficient k of 0.43 ± 0.01 ADC/keV.

The light yield of the BGO crystal is dependent on the temperature. The temperature coefficient of k was measured using the temperature change during a day to be $(-9.2 \pm 1.2) \times 10^{-3}/^{\circ}$C.

The relative energy resolution is estimated as the ratio of the standard deviation σ_E to the deposit energy E_γ, where σ_E was extracted from the calibration peaks. The relation (σ_E/E_γ) is shown in Fig. B.2. The data are fitted to a function of $\sigma_E/E_\gamma = (23.3 \pm 0.1 \text{ MeV}){E_\gamma}^{-1} + (3.02 \pm 0.02) \times 10^{-2}$.

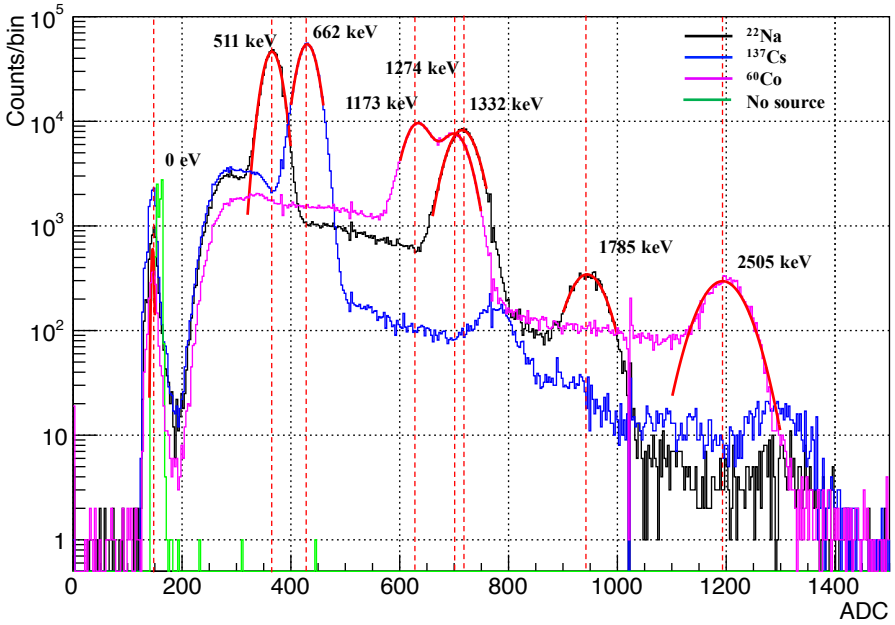

Fig. B.1: Energy calibration of the BGO detector using ^{137}Cs, ^{22}Na, and ^{60}Co.

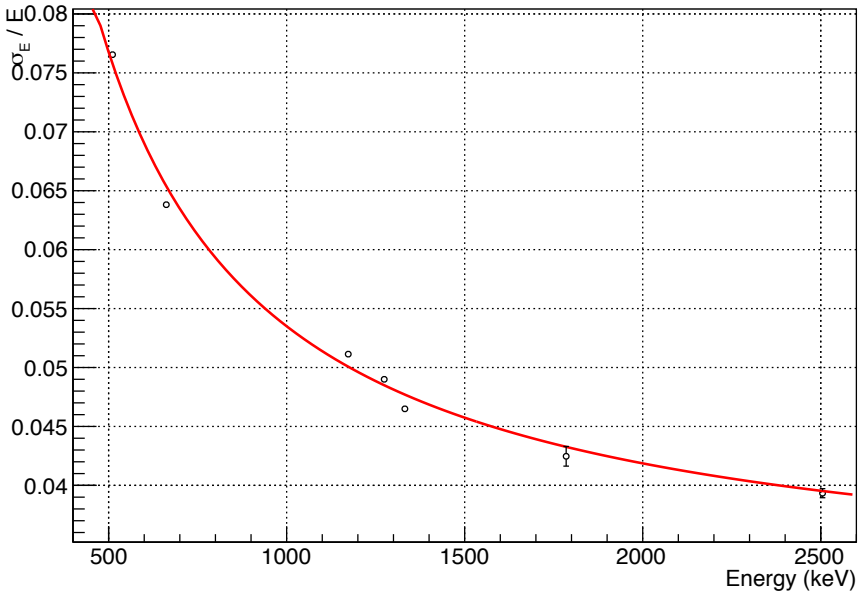

Fig. B.2: Relative energy resolution as a function of energy. The dots are data extracted from the calibration peaks. The red curve is a fit function of $\sigma_{\mathrm{E}}/E_\gamma = (23.3 \pm 0.1\ \mathrm{MeV})/\mathrm{E}_\gamma + (3.02 \pm 0.02) \times 10^{-2}$.

Bibliography

[1] Katsumi Hirose, "Fukushima Daiichi Nuclear Plant accident: Atmospheric and oceanic impacts over the five years", J. Environ. Rad. 157 (2016) 113–130.

[2] Yurika Oba and Toshihiro Yamada, "Sampling design and required sample size for evaluating contamination levels of ^{137}Cs in Japanese fir needles in a mixed deciduous forest stand in Fukushima, Japan", Environ. Pollut. 224 (2017) 430–435.

[3] Hiromi Nabeshi, Tomoaki Tsutsumi, Yoshinori Uekusa, Akiko Hachisuka, Rieko Matsuda and Reiko Teshima, "Surveillance of Strontium-90 in Foods after the Fukushima Daiichi Nuclear Power Plant Accident", Food Hyg. Saf. Sci. 56 (4) (2015) 133.

[4] The Japan Radioisotope Association, "Radioisotope Pocket Data Book 11$^{\text{th}}$ Edition"(2009).

[5] ICRP, "Age-dependence Doses to Members of the Public from Intake of Radionuclides: Part 4 Inhalation Dose Coefficients", ICRP publication 71, 1995.

[6] C. Testa, D. Desideri, F. Guerra, M. A. Meli, C. Roselli, and G. Jia, "The importance of separation chemistry for the determination of radionuclides in environmental samples", J. Radio. Nucl. Chem., 229 (1) (1998) 23–32.

[7] Hideo Hirayama, Kenjiro Kondo, Yasuhiro Unno, Hiroshi Matumura, Hiroshi Iwase, Akira Yunoki, and Shinichi Sasamki, "Rapid and Simple Measurement Method of ^{90}Sr Concentration in Water by Measuring β-rays from ^{90}Y", Trans. Atom. Ener. Soc. Jp., 14 (3) (2015) 141–150.

[8] R. L. Brodzinski, "Portable Instrumentation for Quantitatively Measuring Radioactive Surface Contaminations, Including ^{90}Sr", IEEE Trans. Nucl. Sci., 31 (1) (1984) 686–690.

[9] Hideo Hirayama and Kenjiro Kondo, "Method to Estimate ^{90}Sr/^{90}Y Contamination Density using 70-μm Dose Equivalent Rate", Jpn. J. Health Phys., 50 (4) (2015) 241–248.

[10] D. Brajnik, S. Korpar, G. Medin, M. Staric, A. Stanovnik, "Detection of ^{90}Sr/^{90}Y with Cherenkov radiation", IEEE NSS MIC Conf. Reco. (2) (1995) 840–842.

[11] R. Pestotnik, P. Krizan, S. Korpar, M. Bracko, M. Staric, A. Stanovnik, "Investigation of 90Sr detection with Cherenkov radiation in silica aerogels", IEEE Nuclear Science Symposium Conference Record(1) (2001) 372–374.

[12] R. Pestotnik, I. Dolenc, S. Korpar, P. Krizan, A. Stanovnik, "Cherenkov detector based on aerogel radiator and flat panel PMT for detection of ^{90}Sr", IEEE Nuclear Science Symposium Conference Record (2) (2003) 798–800.

[13] R. Pestotnik, S. Korpar, P. Krizan, A. Stanovnik, "Detection of 90Sr with aerogel Cherenkov detector with low background", IEEE Symposium Conference Record Nuclear Science (1) (2004) 327–329

[14] R. Pestotnik, S. Korpar, P. Krizăn, and R. Dolenec, "Cherenkov detector of 90Sr based on aerogel as radiator", Nucl. Instru. Meth. A, 595 (1) (2008) 278–280.

[15] Y. Saito, Y. Ishii, H. Kawai, Y. Kon, K. Mase, T. Nakano, H. Nakayama, M. Tabata, Y. Tajima, H. Yoshida, M. Yosoi, "Performance evaluation of an electron veto counter with silica aerogel of n ¡ 1.003", IEEE NSS MIC Conf. Reco., (2008) 2456-2458.

[16] Makoto Tabata, "Study of Transparent Silica Aerogel over the Wide Range of Densities", doctor thesis of Chiba Univ. (2009).

[17] T. Sato, H. Kawai, Y. Kishi, M. Kubo, K. Mase, T. Nakano, H. Nakayama, M. Ono, M. Tabata, M. Yosoi, "Development of silica aerogel Cherenkov counter with n = 1.003 for electron veto", IEEE NSS MIC Conf. Reco. (2011) 209–211.

[18] Makoto Tabata, Ichiro Adachi, Hideyuki Kawai, Masato Kubo, Takeshi Sato, "Recent progress in silica aerogel Cherenkov radiator", Phys. Proc., Vol. 37 (2012) 642–649.

[19] Makoto Tabata, Ichiro Adachi, Hideyuki Kawai, Takayuki Sumiyoshi, Hiroshi Yokogawa, "Hydrophobic silica aerogel production at KEK", Nucl. Instr. Meth. A 668 (2012) 64–70.

[20] UNSCEAR 2008 report vol. 1. Source effects and risks of ionizing radiation.

[21] N. Q. Hung, V. H. Hai, M. Nomachi, "Investigation of cosmic-ray induced background of Germanium gamma spectrometer using GEANT4 simulation", App. Rad. Iso.121 (2017) 87–90.

[22] H. Ito, S. Han, A. Kobayashi, N. Kaneko, H. Kawai and M. Tabata, "Identification of ^{90}Sr/^{40}K based on Cherenkov detector for recovery from the Fukushima nuclear accident", JPS Conf. Proc. (2016) 070002.

[23] S. Ijima, S. Han, H. Ito, H. Kawai, S. Kodama, and D. Kumogoshi, "Development of Realtime ^{90}Sr Counter Used in Low Rate Radioactive", IEEE NSS MIC Conf. Reco. (2014) N09-40.

[24] S. Iijima, H. Ito, D. Kumogoshi, K. Satoshi, H. Kawai, M. Tabata, K. Mase, and H. Nakayama, "Development of Realtime 90Sr Counter", IEEE NSS MIC Conf. Reco. (2013) NPO1-169.

[25] Department of Environmental Health and Food Safety Pharmaceutical Safety and Environmental Health Bureau, Ministry of Health, Labour and Welfare, Japan, "Measures to Ensure Food Safety", 2017.

[26] Keith E. Chave, "Chemical Reactions and Composition of Sea Water", J. Chem. Edu., 48 (3) (1971) 148–151.